

広島大学学位請求論文

**Electronic structure and carrier dynamics of ferromagnetic  
shape memory alloys and topological insulators**

強磁性形状記憶合金とトポロジカル絶縁体の電子構造とキャリア  
ダイナミックス

2015年

広島大学大学院理学研究科  
物理学専攻

朱思源  
(Siyuan Zhu)



# 目次

## 1. 主論文

Electronic structure and carrier dynamics of ferromagnetic shape memory alloys and topological insulators

強磁性形状記憶合金とトポロジカル絶縁体の電子構造とキャリアダイナミックス

## 2. 公表論文

(1) Ultrafast electron dynamics at the Dirac node of the topological insulator  $\text{Sb}_2\text{Te}_3$

**S.-Y. Zhu**, Y. Ishida, K. Kuroda, K. Sumida, M. Ye, J. Wang, H. Pan, M. Taniguchi, S. Qiao, S. Shin & A. Kimura

*Scientific Reports* **5**, 13213 (2015)

(2) Drastic change in density of states upon martensitic phase Transition for Metamagnetic Shape Memory Alloy  $\text{Ni}_2\text{Mn}_{1+x}\text{In}_{1-x}$

**S.-Y. Zhu**, M. Ye, K. Shirai, M. Taniguchi, S. Ueda, Y. Miura, M. Shirai, R. Y. Umetsu, R. Kainuma, T. Kanomata and A. Kimura

*Journal of Physics: Condensed Matter* **27**, 362201 (2015)

## 3. 参考論文

(1) Electronic structures and magnetic moments of  $\text{Co}_3\text{FeN}$  thin films grown by molecular beam epitaxy

K. Ito, T. Sanai, **S.-Y. Zhu**, Y. Yasutomi, K. Toko, S. Honda, S. Ueda, Y. Takeda, Y. Saitoh, Y. Imai, A. Kimura, and T. Suemasu

*Applied Physics Letters* **103**, 232403 (2013)

(2) Spectroscopic evidence of band Jahn-Teller distortion upon martensitic phase transition in Heusler-type Ni-Fe(Co)-Ga ferromagnetic shape-memory alloy films

K. Sumida, K. Shirai, **S.-Y. Zhu**, M. Taniguchi, M. Ye, S. Ueda, Y. Takeda, Y. Saitoh, I. Rodriguez, J. M. Barandiarán, V. A. Chernenko, and A. Kimura

*Physical Review B* **91**, 134417 (2015)

(3) X-ray magnetic circular dichroism for  $\text{Co}_x\text{Fe}_{4-x}\text{N}$  ( $x=0, 3, 4$ ) films grown by molecular beam epitaxy

K. Ito, T. Sanai, Y. Yasutomi, **S.-Y. Zhu**, K. Toko, Y. Takeda, Y. Saitoh, A. Kimura and T. Suemasu

*Journal of Applied Physics* **115**, 17C712 (2014)

(4) Quasiparticle interference on the surface of  $\text{Bi}_2\text{Se}_3$  induced by cobalt adatom in the absence of ferromagnetic ordering

M. Ye, S. V. Eremeev, K. Kuroda, E. E. Krasovskii, E. V. Chulkov, Y. Takeda, Y. Saitoh, K. Okamoto, **S.-Y. Zhu**, K. Miyamoto, M. Arita, M. Nakatake, T. Okuda, Y.

Ueda, K. Shimada, H. Namatame, M. Taniguchi and A. Kimura

*Physical Review B* **85**, 205317 (2012)

(5) Perpendicular magnetic anisotropy with enhanced orbital moments of Fe adatoms on a topological surface of  $\text{Bi}_2\text{Se}_3$ .

M. Ye, K. Kuroda, Y. Saitoh, K. Okamoto, **S.-Y. Zhu**, K. Shirai, K. Miyamoto, M. Arita, M. Nakatake, T. Okuda, Y. Ueda, K. Shimada, T. Namatame, M. Taniguchi, A. Kimura

*Journal of Physics: Condense Matter* **25**, 232201 (2013)

(6) Photoelectron Spin-Polarization Control in the Topological Insulator  $\text{Bi}_2\text{Se}_3$

Z.-H. Zhu, C. N. Veenstra, S. Zhdanovich, M. P. Schneider, T. Okuda, K. Miyamoto, **S.-Y. Zhu**, H. Namatame, M. Taniguchi, M. W. Haverkort, I. S. Elfimov, and A. Damascelli

*Physical Review Letters* **112**, 076802 (2014)

# Part I

## 主論文





HIROSHIMA UNIVERSITY

Doctor thesis

---

**Electronic structure and carrier  
dynamics of ferromagnetic shape  
memory alloys and topological  
insulators**

---

Siyuan Zhu

Graduate School of Science  
Hiroshima University

Higashi-Hiroshima  
June, 2015





# Abstract

Since the first industrial revolution in 1760, use of steam energy released people from hard hand production method and greatly improved the workforce productivity. However, as the base of industry, energy consumption is always accompanied with pollution and the cost of resources. Nowadays, due to the increase of population and life quality, the energy consumption have exploded. The growing environmental problems, like haze, dust storm, red tide and so on, reminded us that the pollution and the cost of nonrenewable resources have approached to the limit of our blue planet. One of the most effective solution is to find some low-energy consuming devices. Heusler-type shape-memory alloys and topological insulators(TIs) are two kinds of materials which have shown great potential in this region recently.

Heusler-type ferromagnetic shape-memory alloys exhibiting the first order structural transition are known to show a big magnetocaloric effect. This property is important to realize an environmentally friendly and energy-efficient technology with the potential to outperform conventional gas-compression refrigeration. The structural transition so called martensitic phase transition (MPT) from austenite phase to martensite phase while cooling down and recovers while warming up, is a key property for the big magnetocaloric effect. To address the origin of the MPT, photoemission spectroscopy has been used to unveil the electronic structure. Previously, photoemission studies for  $\text{Ni}_2\text{MnGa}$  and  $\text{Ni}_2\text{Mn}_{1+x}\text{Sn}_{1-x}$  systems have shown that a sharp peak near the Fermi energy, which was attributed to the Ni 3d  $e_g$  minority-spin states, is responsible for the phase transition.  $\text{Ni}_2\text{Mn}_{1+x}\text{In}_{1-x}$  have attracted much more attention due to its giant magneto-resistance and the substantial magnetocaloric effect, which is a key to the magnetic refrigeration at room temperature. Since the excess Mn spin couples parallel to the ordinary Mn spin in  $\text{Ni}_2\text{Mn}_{1+x}\text{In}_{1-x}$ , which is just opposite to the case of  $\text{Ni}_2\text{Mn}_{1+x}\text{Sn}_{1-x}$ , one expect that a different mechanism works for the phase transition. In this work, we have employed hard X-ray photoelectron spectroscopy for the  $\text{Ni}_2\text{Mn}_{1+x}\text{In}_{1-x}$  with  $x=0, 0.12, 0.24$  and  $0.36$ . The sharp peak near the Fermi energy has been observed in the austenite phase and totally disappeared in the martensite phase. In sharp contrast to the  $\text{Ni}_2\text{Mn}_{1+x}\text{Sn}_{1-x}$  system, the shift of this peak as a function of

$x$  was not observed. We have also measured the hysteresis behavior to confirm that the observed change of electronic structure was caused by the structural transition. The results have shown that the increasing/decreasing of the Ni-3d- $e_g$  minority-spin-state peak is strongly related with the structural transition.

Three-dimensional (3D) TIs have gapless surface states protected by time-reversal symmetry. An odd number of massless Dirac cones (a single Dirac cone as the simplest case) with a helical spin texture in momentum space is a manifestation of the 3D TIs. Pure spin current is a key point for the spintronics application, which leads to the fast computation and low-energy consumption. It can be realized on the surface of 3D TIs. Therefore topological insulators have attracted a great attention since discovered. Several topological insulators, like  $\text{Bi}_2\text{Se}_3$ ,  $\text{Sb}_2\text{Te}_3$ ,  $\text{Bi}_2\text{Te}_3$  and  $\text{TlBiSe}_2$ , have been experimentally realized. For the moment, most of the materials are studied in equilibrium. However, for application, hot carrier dynamics is also necessary, especially for the Dirac fermions. In the second part of thesis, we studied the ultrafast electron dynamics of  $\text{Sb}_2\text{Te}_3$  with the time-resolved angle-resolved photoemission spectroscopy (TrARPES). Previously, due to the limit of energy resolution, it is difficult to study the dynamics of Dirac fermions. In this study, with rather high energy resolution and suitable candidate  $\text{Sb}_2\text{Te}_3$ , we have observed the dynamics of Dirac fermions successfully. As usual, higher energy region always shows earlier intensity peak. Interestingly, we have found that the intensity peak of higher Dirac cone is later than that of lower Dirac cone, just like jammed near the Dirac node. We have named it as hourglass effect and pointed out that the low density of state near Dirac node is responsible for this effect. Then we can conclude that hourglass effect will occur for all the materials which have isolated Dirac cone and unoccupied Dirac node. As isolated Dirac cone is necessary for the application of spintronics device, hourglass effect shows great importance for further research.

Except for electron dynamics, magnetism is also an important case for TIs. Magnetically doped TIs can open an energy gap at the Dirac point by breaking time-reversal-symmetry. It will lead to the quantized anomalous Hall (QAH) effect, which shows a great potential in the development of low-energy-consuming devices

using electron spins. Though several candidates of magnetically doped TIs have been demonstrated to show long-range magnetic order, QAH are realized only in the Cr/V-doped  $(\text{Sb,Bi})_2\text{Te}_3$  systems. In the third part of thesis, we have studied the elemental specified magnetic properties of magnetic doped topological insulator  $\text{V}_{0.018}\text{Sb}_{1.98}\text{Te}_3$  with X-ray magnetic circular dichroism (XMCD). We have found that long-range magnetic order is mediated by the p-hole carriers of the host lattice, and the interaction between the Sb(Te)  $p$  and V  $d$  states is crucial. The easy axis is perpendicular to the sample surface, which shows advantage for the realization of QAH.



# Contents

<b>List of figures</b>	<b>7</b>
<b>1 Introduction</b>	<b>9</b>
1.1 Preface . . . . .	9
1.2 Purpose . . . . .	10
1.3 Outline . . . . .	11
<b>2 Background</b>	<b>12</b>
2.1 Electronic structure and carrier dynamics of materials . . . . .	12
2.2 Ferromagnetic shape memory alloys . . . . .	12
2.3 Topological insulator . . . . .	15
2.4 Quantum anomalous Hall effect . . . . .	16
<b>3 Experimental techniques</b>	<b>20</b>
3.1 Photoelectron spectroscopy . . . . .	20
3.1.1 Synchrotron radiation . . . . .	20
3.1.2 Hard X-ray photoelectron spectroscopy . . . . .	20
3.1.3 Angle-resolved photoelectron spectroscopy . . . . .	22
3.1.4 Time-resolved angle-resolved photoelectron spectroscopy . . . . .	23
3.2 XMCD . . . . .	25
<b>4 Drastic Change in Density of States upon Martensitic Phase Transition for Metamagnetic Shape Memory Alloy <math>\text{Ni}_2\text{Mn}_{1+x}\text{In}_{1-x}</math></b>	<b>26</b>
4.1 Introduction . . . . .	26
4.2 Experimental method . . . . .	27
4.3 Results and discussion . . . . .	27
4.4 Conclusion . . . . .	34
<b>5 Ultrafast electron dynamics at the Dirac node of the topological insulator <math>\text{Sb}_2\text{Te}_3</math></b>	<b>36</b>
5.1 Introduction . . . . .	36

5.2	Experimental method . . . . .	37
5.3	Results and discussion . . . . .	37
5.3.1	Experimental results . . . . .	37
5.3.2	simulation . . . . .	42
5.4	Conclusion . . . . .	45
<b>6</b>	<b>X-ray magnetic circular dichroism study of ferromagnetic topological insulator V-doped <math>\text{Sb}_2\text{Te}_3</math></b>	<b>46</b>
6.1	Introduction . . . . .	46
6.2	Experimental method . . . . .	47
6.3	Experimental results and discussion . . . . .	48
6.4	Conclusion . . . . .	49
<b>7</b>	<b>Summary</b>	<b>51</b>
	<b>Acknowledgement</b>	<b>52</b>
	<b>References</b>	<b>53</b>

## List of Figures

1	Relationship between electronic structure and conductivity. . . . .	12
2	Schematic diagram of the structure change in martensite phase transition	13
3	Recovery strain caused by MPT for $\text{Ni}_{45}\text{Co}_5\text{Mn}_{36.7}\text{In}_{13.3}$ at room temperature . . . . .	14
4	Temperature dependent magnetization and adiabatic process for $\text{Ni}_{50}\text{Mn}_{34}\text{In}_{16}$ alloys . . . . .	14
5	Adiabatic temperature change $\Delta T_{ad}$ for several materials . . . . .	15
6	Schematic diagram of 2D and 3D topological insulator . . . . .	16
7	Schematic figure of Hall effect . . . . .	17
8	Hall resistivity depending on the applied magnetic field for integer Quantum Hall effect . . . . .	18
9	Hall resistivity depending on the applied magnetic field for fraction Quantum Hall effect . . . . .	18
10	Schematic diagram of synchrotron radiation system . . . . .	20
11	Schematic diagram of hard X-ray photoemission spectroscopy . . . . .	21
12	Schematic diagram of BL15XU . . . . .	22
13	Schematic diagram of ARPES . . . . .	23
14	Schematic diagram for principle of trARPES . . . . .	24
15	Schematic diagram of trARPES system . . . . .	24
16	Schematic diagram for principle of XMCD . . . . .	25
17	Photoelectron spectra of $\text{Ni}_2\text{Mn}_{1+x}\text{In}_{1-x}$ ( $x=0, 0.12, 0.24$ and $0.36$ ) at different temperature . . . . .	29
18	Cooling and warming processes of $\text{Ni}_2\text{Mn}_{1+x}\text{In}_{1-x}$ ( $x=0.36$ ) . . . . .	30
19	Calculated DOS of $\text{Ni}_2\text{Mn}_{1+x}\text{In}_{1-x}$ ( $x=0, 0.25,$ and $0.5$ ) . . . . .	32
20	Total energy difference as a function of the axial ration $c/a$ . . . . .	33
21	The electronic structure of $\text{Sb}_2\text{Te}_3$ . . . . .	38
22	The time dependent study of $\text{Sb}_2\text{Te}_3$ spectra . . . . .	39

23	Decay behaviors of bulk and surface states . . . . .	40
24	The schematic figures of the pump and decay processes . . . . .	43
25	Simulation of decay behavior from thermal distribution . . . . .	44
26	Simulation of a simple model for hourglass effect . . . . .	44
27	Element specific magnetic moment of $V_{0.018}Sb_{1.98}Te_3$ . . . . .	48
28	M-T curve and magnetic anisotropy . . . . .	49



# 1 Introduction

## 1.1 Preface

Spin of electrons in condensed matter lead to many novel phenomena, including ferromagnetic shape-memory alloy, topological insulators, superconductors, giant magneto-resistance, electron paramagnetic resonance and so on. Magnetic refrigeration based on the magnetocaloric effect (MCE) was considered to be an environmentally friendly and energy-efficient technology with the potential to outperform conventional gas-compression refrigeration for applications [2, 3]. For realizing the magnetic refrigeration, room-temperature giant magnetocaloric compounds are necessary. Recently, Ni-Mn-(In, Sn, Sb)-based magnetic shape-memory alloys have been reported to be solid-state refrigerants with the large magnetocaloric effect [7, 8]. Furthermore, the Ni-Mn-In system with non-toxic elements showed the large cooling span, single-phase nature and oxidation resistance, which are suitable for application.

Topological insulators in two or three dimensions have insulating energy gaps in the bulk, and gapless edge or surface states at the sample boundary that are protected by time-reversal symmetry. The pure spin current induced at edges or surfaces of topological insulators is a key point for realizing quantum computer, which can increase the computing speed by several thousand times. Electron dynamics are important for expanding our knowledge of topological insulator. Even though there are many studies on the electron dynamics of topological insulators, due to the limited energy resolution, electron dynamics in the vicinity of Dirac node is unknown. As an important step for application, the Quantum anomalous Hall effect (QAHE) has been predicted in 2008 and experimentally realized in 2013. The realizing method is to break the time-reversal symmetry by doping magnetic element. Although many materials have been expected to show QAHE, it has been realized only in V- and Cr-doped  $\text{Bi}_x\text{Sb}_{2-x}\text{Te}_3$ . Therefore, magnetic property of magnetic doped topological insulator should be studied for expanding the understanding of QAHE.

## 1.2 Purpose

Firstly, for FSMA, with hard X-Ray photoelectron spectroscopy employed, role of electronic structure played in the martensite phase transition was studied. A sharp peak near the Fermi energy  $E_F$  has also been reported for  $\text{Ni}_2\text{MnGa}$  and  $\text{Ni}_2\text{Mn}_{1+x}\text{Sn}_{1-x}$ . This peak is attributed to the Ni  $3d e_g$  minority-spin and has been proposed to be strongly related to the structural transition [9–11, 27, 38]. To study the electronic structure of Ni-Mn-In system, we firstly compared it with the Ni-Mn-Sn system. In the Ni-Mn-based Heusler alloys, the magnetic moment is confined to the Mn atoms to a large extent [12]. In  $\text{Ni}_2\text{Mn}_{1+x}\text{Sn}_{1-x}$  system, due to the hybridization between the Ni  $3d e_g$  states and the  $3d$  states of excess Mn atoms at Sn site, the peak structure composed of the minority-spin  $3d e_g$  states in the high temperature cubic phase shows a systematic energy shift towards Fermi Energy with increasing  $x$ . According to the first-principles calculation, the hybridization plays an important role in driving the instability of the cubic phase [27]. However, in  $\text{Ni}_2\text{Mn}_{1+x}\text{In}_{1-x}$  system the  $3d$  states of excess Mn atoms have been predicted to be majority-spin, which is opposite to that in  $\text{Ni}_2\text{Mn}_{1+x}\text{Sn}_{1-x}$  system [13]. Therefore the hybridization will not appear in  $\text{Ni}_2\text{Mn}_{1+x}\text{In}_{1-x}$  system and there should be some other force driving the instability of the cubic phase. In this case, further study of  $\text{Ni}_2\text{Mn}_{1+x}\text{In}_{1-x}$  system is necessary.

Secondly, topological insulators are a new quantum state of matter. Their lineae surface state leads to massless Dirac fermions and ultrahigh mobility. Spin current is also hopeful to be realized in topological insulator. Investigation of fermion dynamics near the Dirac point is crucial for the future development of spintronic devices incorporating topological insulators. However, research so far has been unsatisfactory because of a substantial overlap with the bulk valence band and a lack of a completely unoccupied Dirac node. Here, we explore the surface Dirac fermion dynamics in the topological insulator  $\text{Sb}_2\text{Te}_3$  by time- and angle-resolved photoemission spectroscopy (TrARPES).  $\text{Sb}_2\text{Te}_3$  has a Dirac node completely located above the Fermi energy with an in-gap Dirac node. With rather high energy resolution ( $\sim 20\text{meV}$ ), we could study the electron dynamics near Dirac node.

Thirdly, QAHE is an important phenomena for the application of topological

insulators. For the moment, QAHE is only realized in V- and Cr-doped  $\text{Bi}_x\text{Sb}_{2-x}\text{Te}_3$ . As QAHE is realized by breaking the time-reversal symmetry, magnetic doping should be the key point. To understand the elemental specified magnetic property, XMCD is the most effective method.

### 1.3 Outline

In Chapter 2, the backgrounds of FSMA and TIs will be introduced. In Chapter 3, the main experimental techniques, hard X-ray photoelectron spectroscopy, time- and angle- resolved photoelectron spectroscopy and XMCD will be described. Chapter 4 will introduce the work on FSMA Ni-Mn-In and explain the origin of MPT in this system. Chapter 5 is devoted to the trARPES of topological insulator  $\text{Sb}_2\text{Te}_3$  and the ultrafast electron dynamics near Dirac node is studied. Chapter 6 includes the magnetic property of V-doped  $\text{Sb}_2\text{Te}_3$  studied by XMCD. Finally, the present study is summarized in Chapter 7.

## 2 Background

### 2.1 Electronic structure and carrier dynamics of materials

As we know, electronic structure is important for materials. Figure 1 shows that as the energy gap between conduction band and valence band decreases, material goes from insulating to semiconducting. If the fermi energy crosses the conduction band, it becomes a conductor. Not only the conductivity of material, but also thermal conductivity, stability, magnetic property, hardness etc. are driven by the electronic structure. Therefore, we can say that electronic structure is the soul of materials. As many functional materials have been discovered in these years, understanding of their underlying mechanism in terms of electronic structure is very important. It will help us for designing materials. Furthermore, for application, carriers travel along the devices.

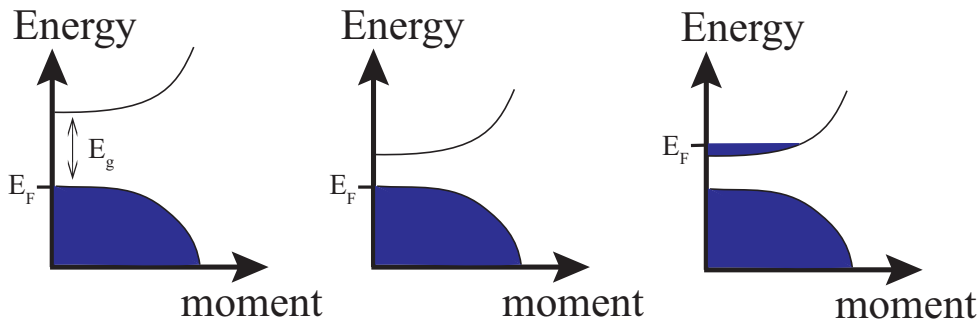


Figure 1: Relationship between electronic structure and conductivity.

Such electron transport phenomena could be fully understood from inequilibrium carrier dynamics, whose decay might occur through electron-phonon and/or electron-electron interaction.

### 2.2 Ferromagnetic shape memory alloys

Conventional magnetic materials are heated up when they are placed in a magnetic field due to a decrease of entropy and cooled down when they are removed adiabatically. This phenomenon is known as the magnetocaloric effect (MCE) [1]. MCE can be applied for realizing magnetic refrigeration, which has been used for reaching sub-Kelvin temperatures by operating with paramagnetic salts [2]. To get magnetic refrigeration which can be used for daily life, we expect to have giant magnetocaloric compounds

which can work at room-temperature. Therefore, a big change of magnetization near room-temperature is necessary. Some room-temperature giant magnetocaloric compounds has been discovered with a structural transition. It is considered to be an environmental friendly and energy-efficient technology [3]. The structural transition is called martensite phase transition (MPT), as shown in Figure 2(a).

In 1996, a new member of Heusler alloys, so-called the ferromagnetic shape memory alloy (FSMA) Ni-Mn-Ga with a large magnetic field-induced strain was discovered [4, 5]. Currently, the Mn-based full Heusler alloys with the generic formula  $X_2MnZ$  with X being a 3d metal and Z belonging to the III or IV group are well known magnetic systems displaying the highest magnetic moment of up to  $5\mu_B$  confined to manganese atoms [6]. In 2006, metamagnetic shape-memory effect was introduced [7]. In their work,

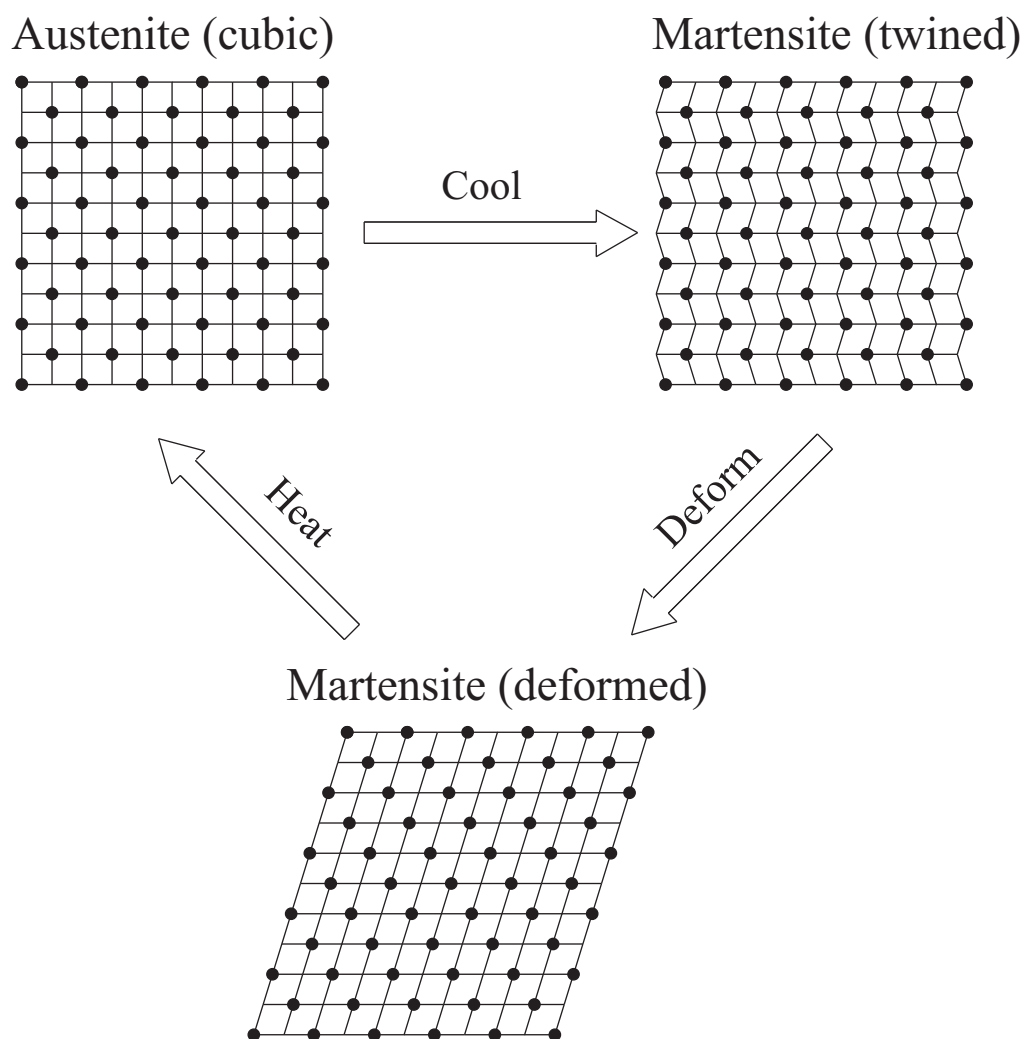


Figure 2: Schematic diagram of the structure change in martensite phase transition.

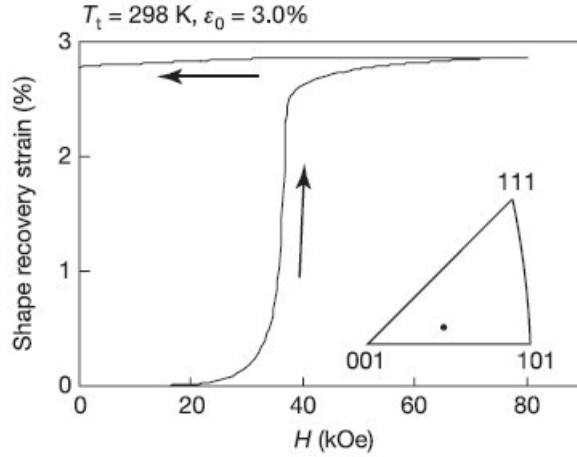


Figure 3: Recovery strain caused by MPT for  $\text{Ni}_{45}\text{Co}_5\text{Mn}_{36.7}\text{In}_{13.3}$  at room temperature [7]. Reprinted by permission from Macmillan Publishers Ltd: [Nature] (Ref. 7), copyright (2006).

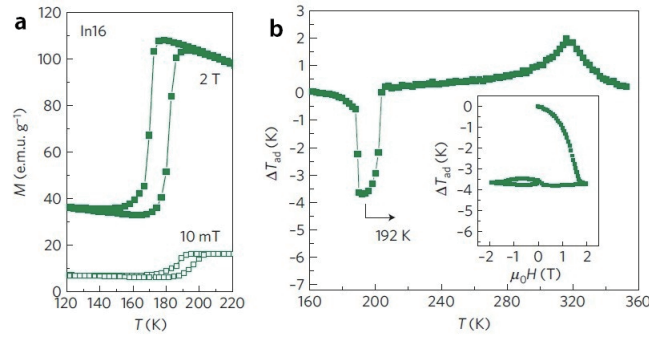


Figure 4: Giant cooling effect and tunable adiabatic temperature for  $\text{Ni}_{50}\text{Mn}_{34}\text{In}_{16}$  alloys. (a) Temperature dependent magnetization at 2 T and 10 mT. (b) Temperature dependent adiabatic temperature change ( $\Delta H = 1.9T$ ). The insets show adiabatic temperature change via magnetic field [8]. Reprinted by permission from Macmillan Publishers Ltd: [Nature Materials] (Ref. 8), copyright (2012).

a compressive pre-strain of about 3% was obtained in the  $\text{Ni}_{1.80}\text{Co}_{0.20}\text{Mn}_{1.47}\text{In}_{0.53}$  alloy. The shape recovery is explained by the magnetic-field induced reverse transformation, which is called the meta magnetic shape-memory effect [7].

Recently, alloys of  $\text{Ni}_2\text{Mn}_{1+x}\text{In}_{1-x}$  have been proposed to have a large magnetocaloric effect and associated giant cooling effect [8]. The giant cooling effect comes from the large magnetization drop from austenite phase to martensite phase. Considering an adiabatic process, latent heat  $\Delta Q$  from one phase to another can be written as  $\Delta Q = C_P \Delta T_{ad}$ , where  $C_P$  and  $\Delta T_{ad}$  denote the heat capacity and adiabatic temperature change, respectively. Considering an isothermal process  $\Delta Q = T_P \Delta S$ . Here  $T_P$  is

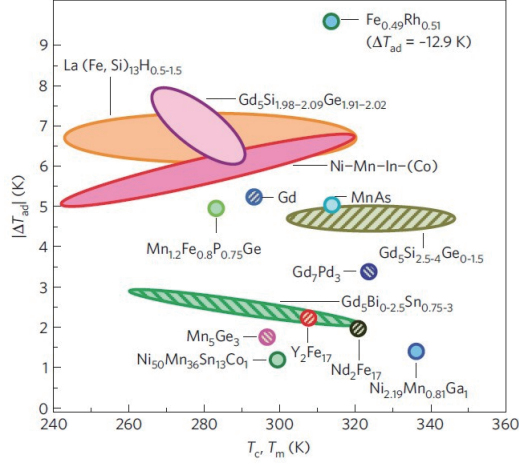


Figure 5: Adiabatic temperature change  $\Delta T_{ad}(\Delta H = 2T)$  as a function of temperature for several materials showing potential in the application of magnetic refrigerants [8]. Reprinted by permission from Macmillan Publishers Ltd: [Nature Materials] (Ref. 8), copyright (2012).

the transition temperature and  $\Delta S$  is the change of entropy. Then an adiabatic temperature change is expressed as  $\Delta T_{ad} = \frac{T_P}{C_P} \Delta S$ . With Clausius-Clayperon equation  $\Delta S = \frac{dH}{dT_P} \Delta M = \Delta M / m$ , where  $\Delta M$  means the difference in magnetization and  $m$  means the change of transition temperatures by applied field, we can find that the change of adiabatic temperature  $\Delta T_{ad}$  depends on the difference in magnetization. Comparing with other materials, the  $\text{Ni}_2\text{Mn}_{1+x}\text{In}_{1-x}$  system with giant cooling effect shows great potential for application. Even though there are still some materials shows larger adiabatic temperature, the  $\text{Ni}_2\text{Mn}_{1+x}\text{In}_{1-x}$  system shows some other advantages, like the large cooling span, non-toxic elements, single-phase nature, oxidation resistance and so on. For  $\text{Fe}_{0.49}\text{Rh}_{0.51}$  and  $\text{Gd}_5\text{Si}_2\text{Ge}_2$  system, the cooling span is smaller, and for  $\text{La}(\text{Fe}, \text{Si})_{13}\text{H}_{0.5-1.5}$  system, the oxidation resistance is not so good [8].

### 2.3 Topological insulator

Three-dimensional topological insulator (TI) is a kind of material which shows potential for realizing pure spin current. As the most important character of TI, nontrivial gapless surface states (SS) is generated by a strong spin-orbit coupling. As shown in Figure 6 (a) and (b), the spin current appears at the edge and surface of 2D and 3D topological insulator. Figure 6 (c) shows the typical band dispersion of topological insulator. The

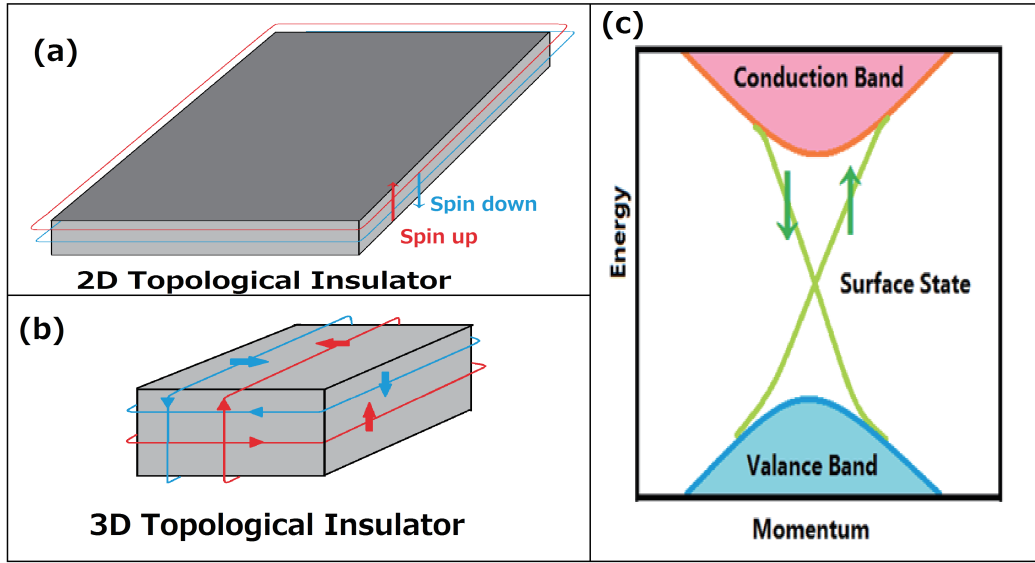


Figure 6: Schematic diagram of topological insulators. (a) Spin current at the edge of 2D topological insulator (b) Spin current on the surface of 3D topological insulator (c) Schematic diagram of band dispersion in topological insulator

gapless surface state is formed with two branches which show opposite spin-polarization.

The SS traversing the band gap between the bulk valence band (VB) and conduction band (CB) can be described by the Dirac equation for massless fermions [40–44]. Additionally, the SS are spin-polarized and the spin orientations are fixed with respect to their momenta [45–47]. Such a peculiar electronic structure, which originates from its  $\pi$  Berry phase, results in an anti-localization of surface electrons with a suppressed backscattering probability. A number of 3D TIs, including  $\text{Bi}_2\text{Se}_3$ ,  $\text{Bi}_2\text{Te}_3$ ,  $\text{Sb}_2\text{Te}_3$ ,  $\text{TlBiSe}_2$ ,  $\text{PbBi}_2\text{Te}_4$  and  $\text{SnSb}_2\text{Te}_4$ , have been discovered experimentally [48–52]. TIs have recently attracted much attention because of their possible applications in spintronic devices and in ultra-fast and fault tolerant quantum computation [53–56]. When aiming to improve such novel device applications incorporating TIs, it is important to understand the hot carrier dynamics of the surface Dirac fermions.

## 2.4 Quantum anomalous Hall effect

Hall Effect was defined as below: The production of a voltage difference (the Hall voltage) across an electrical conductor, transverse to an electric current in the conductor and a magnetic field perpendicular to the current. Hall voltage  $V_H = -IB/net$ , where



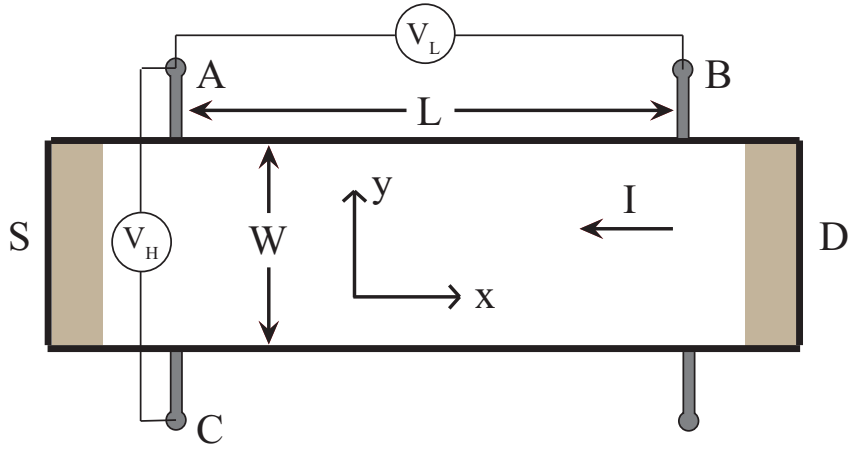


Figure 7: Schematic figure of Hall effect.

$I$  is the current across the plate length,  $B$  is the magnetic field,  $t$  is the thickness of the plate,  $e$  is the elementary charge, and  $n$  is the charge carrier density of the carrier electrons. Hall coefficient is defined as

$$R_H = E_y/(j_x B)$$

, where  $j_x$  is the current density of the carrier electrons, and  $E_y$  is the induced electric field.

$$R_H = E_y/(j_x B) = (V_H t)/IB = -1/ne$$

By measuring the Hall coefficient  $R_H$ , carrier density can be evaluated. Figure 7 shows the schematic figure of Hall effect.

For ferromagnetic materials (and paramagnetic materials in a magnetic field), the Hall resistivity includes an additional contribution, known as the anomalous Hall effect. Anomalous Hall effect is often much much larger than the ordinary Hall effect and strongly related to the magnetization of the material.

The quantum Hall effect has been observed in an extreme condition such as under a strong magnetic field at very low temperature. In this system, Landau levels must be considered. To simplify the effect, we use the value  $i$  to separate the effects.  $R_H = \frac{V_H}{I} = -\frac{1}{i} \frac{h}{e^2}$ . For integer Quantum Hall effect,  $i$  is integer, as shown in Figure 8. For fraction Quantum Hall effect,  $i$  is fraction ( $i = 1/3, 2/5, 3/7, 4/9$ ), as shown in Figure 9.

Topological insulators are nonmagnetic insulators with novel surface states that are a consequence of the nontrivial topology of electronic wave functions in the bulk of the

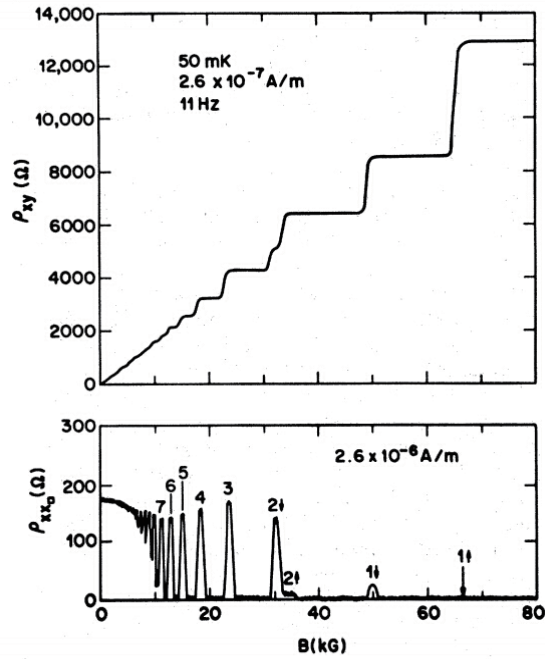


Figure 8: Hall resistivity depending on the applied magnetic field for integer Quantum Hall effect [16]. Figures reprinted with permission from Ref. 16 (©1982, American Physical Society)

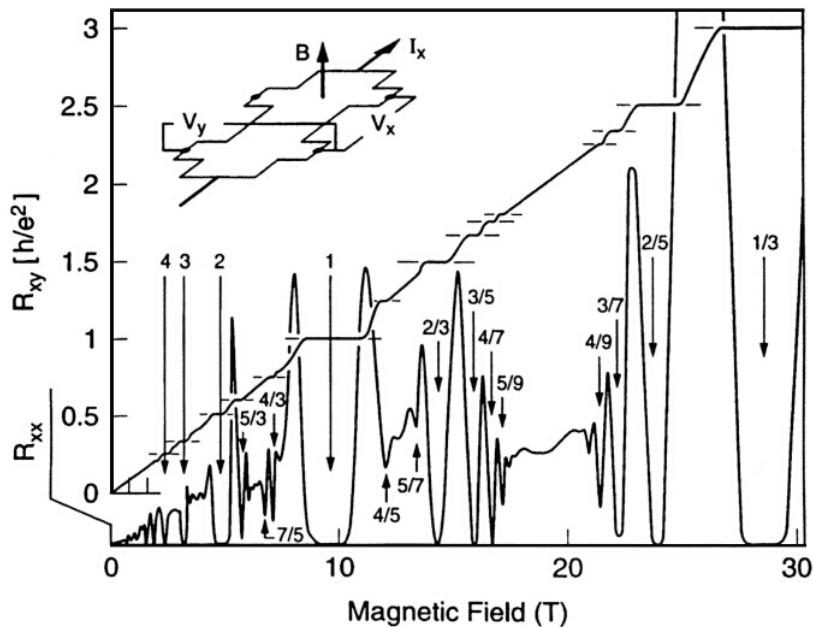


Figure 9: Hall resistivity depending on the applied magnetic field for fraction Quantum Hall effect (The data was taken in GaAs at  $T = 85$  mK) [17]. Figures reprinted with permission from Ref. 17 (©1999, American Physical Society)

materials. The surface state will allow spin current appears at the edge of 2D topological insulators. This is called quantum spin Hall effect. The quantized Hall conductance is given by a topological characteristic of the band structure. It is known as the first Chern number.

Magnetization will break the time reversal symmetry of TI, which is the base of Quantum Anomalous Hall(QAH) effect. It is considered as the quantized version of the conventional anomalous Hall Effect which was discovered in 1881. The quantized version of the anomalous Hall effect has been predicted to occur in magnetic topological insulators, but the experimental realization has been challenging [14]. In 2013, the observation of the quantum anomalous Hall (QAH) effect is realized in thin films of Cr-doped  $(\text{Bi,Sb})_2\text{Te}_3$ , a magnetic topological insulator [15]. At zero magnetic field, the gate-tuned anomalous Hall resistance reaches the predicted quantized value of  $h/e^2$ , accompanied by a considerable drop of the longitudinal resistance. Under a strong magnetic field, the longitudinal resistance vanishes whereas the Hall resistance remains at the quantized value [15]. The realization of the QAH effect may lead to the development of low-power-consumption electronics.

## 3 Experimental techniques

### 3.1 Photoelectron spectroscopy

#### 3.1.1 Synchrotron radiation

When charged particles are accelerated radially, we will have electromagnetic radiation along the tangential direction. This radiation is called synchrotron radiation, as shown in Figure 10 (a). There are several advantages of the synchrotron radiation:

1. Broad spectrum: from microwaves to hard X-rays
2. High flux: the high intensity photon beam allows rapid experiment
3. High brilliance: highly collimated photon beam leads to small light size and spatial coherence
4. High stability
5. Polarization: polarization can be both linear and circular

Synchrotron radiation can be provided by bending magnets or undulators. Schematic diagram is shown in Figure 10 (b) and (c). Compared with bending magnets, For an undulator with  $N$  periods, the brightness can be up to  $N^2$  times to the bending magnet. With a well-designed undulator, the brightness can be increased to over  $10^5$  times.

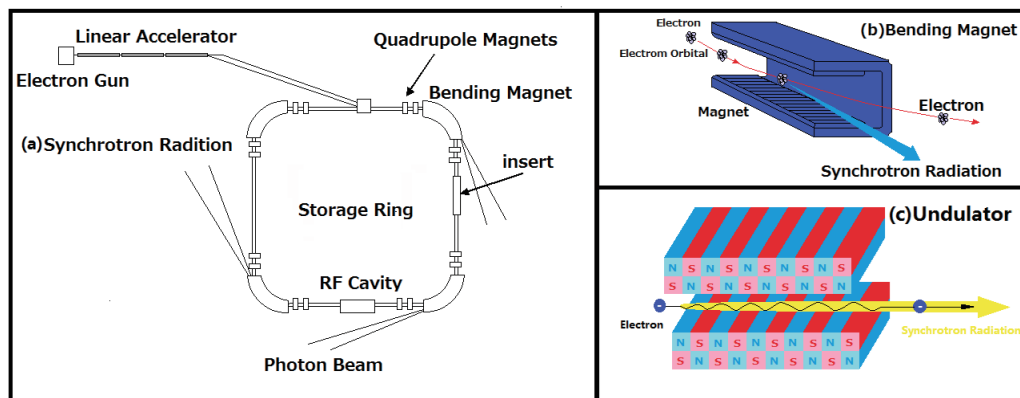


Figure 10: Schematic diagram of (a) synchrotron radiation (b) bending magnets and (c) undulator.

#### 3.1.2 Hard X-ray photoelectron spectroscopy

Photoelectron spectroscopy(PES) is based on the photoelectric effect, as shown in Figure 11. When the sample irradiated by light, electrons inside the material are emitted

into vacuum. Here for the occupied state, the vertical axis corresponds to binding energy. Valence band and core levels are marked by red and blue colors, respectively. From energy conservation law,  $E_B = \hbar\omega - E_{kf} - \phi$ , here  $E_B$  is binding energy of the electron,  $\hbar\omega$  is incoming photon energy,  $E_k$  is kinetic energy of the outgoing electron and  $\phi$  is the electron work function. When we have constant photon energy, the energy of emitted electrons reflects the energy of their original states in the material. Then we collect the electrons with the electrostatic hemispherical analyzer. By tuning the voltage between two plates, kinetic energy of electrons arriving to the detector can be selected. By measuring the number of photoelectrons as a function of kinetic energy, we obtain a spectrum as shown in Figure 11. This spectrum reflects the occupied density of states of materials. With this method, the occupied electronic structures can be directly observed by PES.

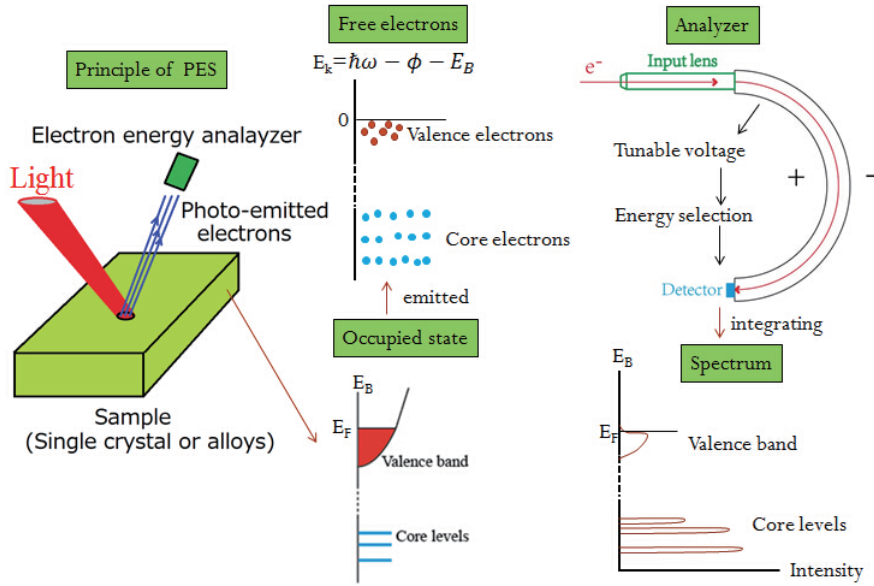


Figure 11: Schematic diagram of hard X-ray photoemission spectroscopy.

In our work, we choose hard X-ray as the light source. Therefore, it is called hard X-ray photoelectron spectroscopy. Hard X-ray is the light with a photon energy larger than several thousand electron volt. With such a high energy, a probing depth around 5nm can be obtained. It leads to the bulk sensitive measurement, which is necessary for Heusler alloys.

Hard X-Ray photoemission spectroscopy measurement was taken by using BL-15

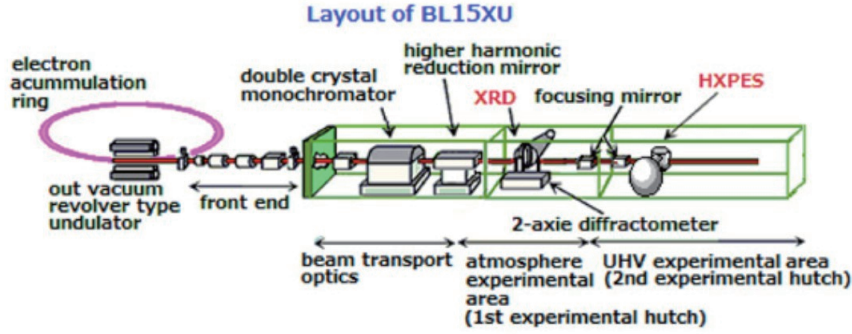


Figure 12: Schematic diagram of BL15XU (From homepage of SPring-8. URL: [http://www.spring8.or.jp/wkg/BL15XU/instrument/lang/INS-0000000451/instrument\\_summary\\_view](http://www.spring8.or.jp/wkg/BL15XU/instrument/lang/INS-0000000451/instrument_summary_view)).

in SPring-8, as shown in Figure 12. The first experiment hutch (XRD) has not been employed in our experiment. Photon Energy of 6000eV was employed in the experiment. Energy resolution was better than 300meV. All of the measurements were performed in ultrahigh vacuum (better than  $2 \times 10^{-7}$  Pa).

### 3.1.3 Angle-resolved photoelectron spectroscopy

Angle-resolved photoemission spectroscopy (ARPES) is the most effective experimental technique for observing the band dispersion of materials in the reciprocal space. It is necessary for studying the electronic structure of solids. ARPES gives information on the direction, speed and amount of electrons in the sample studied. So we can get both the energy and momentum of an electron, which provide us with detailed information on the band dispersion and the Fermi surface. The schematic diagram is shown in Figure 13.

First of all, considering photoelectric effect, from energy conservation law,  $E = \hbar\omega - E_{kf} - \phi$ . Here  $E$  is binding energy of the electron,  $\hbar\omega$  is incoming photon energy,  $E_k$  is kinetic energy of the outgoing electron and  $\phi$  is the work function. Work function  $\phi$  only depends on the sample and  $\hbar\omega$  can be a constant by controlling the light. Therefore, if we can observe the kinetic energy  $E_k$ , the binding energy of electrons inside the material can be obtained easily.

Secondly, comparing with electron momentum, photon momentum is small enough for neglecting. Therefore, the component of electron momentum in the plane of sample

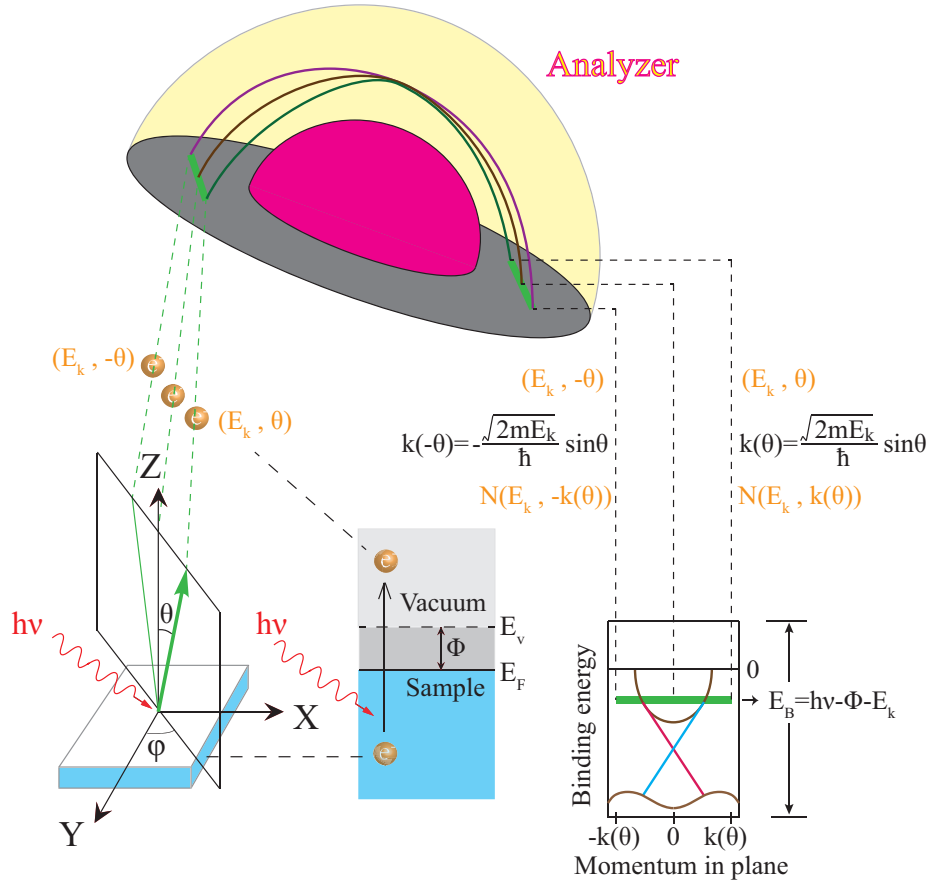


Figure 13: Schematic diagram of ARPES.

$K_{\parallel}$  can be considered to be constant before and after emitted. Then we can have an equation  $\hbar K_{\parallel} = \sqrt{2mE_k} \sin\theta$ , where  $m$  is the mass of an electron and  $\theta$  is the angle between out going electron and the out of plane direction. From this equation, we find that electron momentum in plane can be obtained from the angle  $\theta$  and kinetic energy  $E_k$ .

As shown in Figure 13, the angle  $\theta$  and kinetic energy  $E_k$  can be specified with a hemispherical electron energy analyzer. By integrating the number of electrons at different energies and angles, we can observe the band dispersion of single crystal (or thin film) by ARPES.

### 3.1.4 Time-resolved angle-resolved photoelectron spectroscopy

Time-resolved ARPES is realized with an ultrafast pump-and-probe method. As shown in Figure 14(a), a pulsed laser source is applied to provide the laser pulses with variable delay time. One pulse with photon energy  $\hbar\omega$  was used for pump and the other pulse

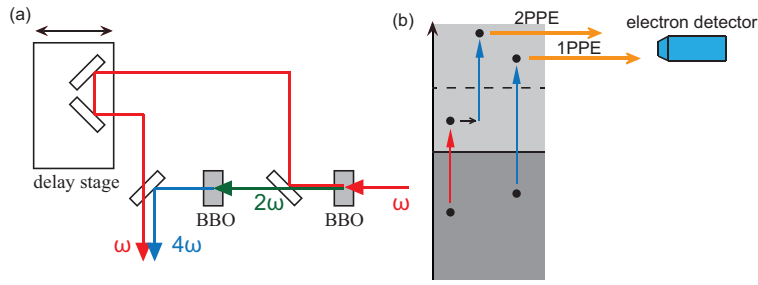


Figure 14: Schematic diagram for principle of trARPES.

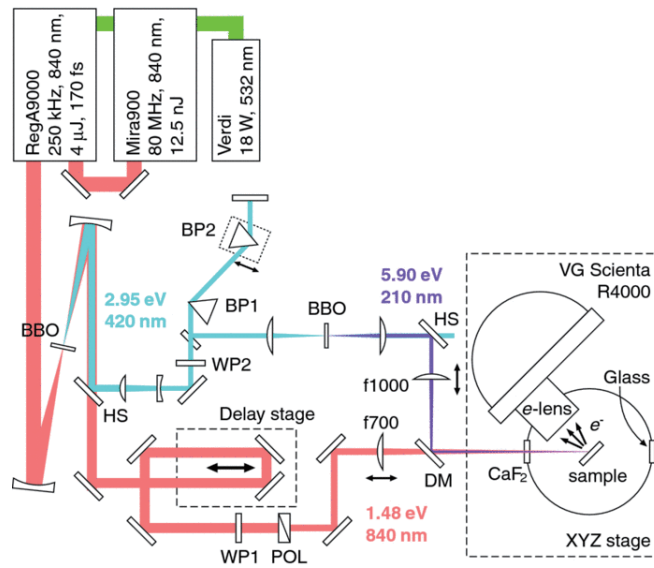


Figure 15: Schematic diagram of trARPES system [69]. Figures reprinted with permission from Ref. 69 (©2014 AIP Publishing LLC)

with photon energy  $4\hbar\omega$  was used for probe, as shown in Figure 14(b). Controlling the delay time by moving the stage, we can observe the unoccupied states and hot carrier dynamics.

The more detailed information of the trARPES system is shown in Figure 15. Two  $\lambda/2$  wave plates are marked as WP1 and WP2. They are used for controlling polarization together with a polarizer (POL). BBO means the Beta Barium Borate ( $\beta$ -BaB<sub>2</sub>O<sub>4</sub>), which is the frequency doubling crystal. HS means the Dielectric mirror, which reflects the light with specified photon energy. Pol means polarizer which passes light of a specific polarization and blocks waves of other polarizations. Prism compressor is used for shortening the duration of pulse by giving different wavelength components a different delay time. Delay stage is employed for controlling the delay time of pump laser.



### 3.2 XMCD

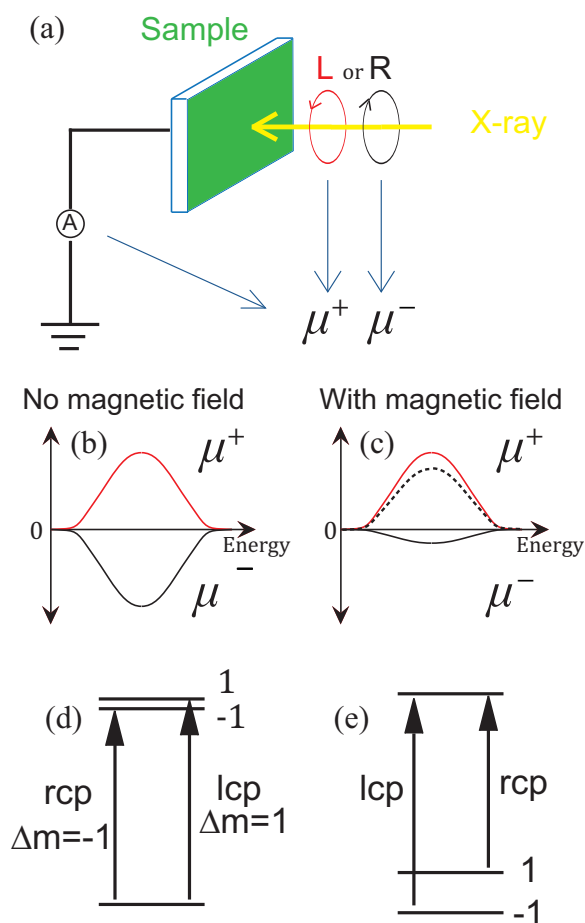


Figure 16: Schematic diagram for principle of XMCD.

A circular dichroism (CD) is defined as a difference in the absorption coefficients excited by left- and right- handed circularly polarized light. The magnetic materials whose macroscopic magnetization is aligned parallel and antiparallel to the incident photon spin produces CD. In the soft- and hard- X-ray regime, one can excite the electron from the core-level into the conduction band. The CD for the magnetized sample in a core absorption excitation region is called X-ray magnetic circular dichroism (XMCD), as shown in Figure 16. By analysing the XMCD spectrum, the information on spin and orbital magnetic moment can be obtained in a site specific manner.

# 4 Drastic Change in Density of States upon Martensitic Phase Transition for Metamagnetic Shape Memory Alloy $\text{Ni}_2\text{Mn}_{1+x}\text{In}_{1-x}$

## 4.1 Introduction

After its discovery in 1984 [18], the ferromagnetic shape memory alloy (FSMA) Ni-Mn-Ga has attracted a great deal of attention because of a large magnetic field-induced strain of about 12% owing to MPT [19–21]. Recently, a new family of the Heusler-based FSMAs  $\text{Ni}_2\text{Mn}_{1+x}\text{Z}_{1-x}$  (Z=In, Sn, Sb) has been discovered [7, 12, 22]. One of the key properties of these alloys is attributed to the steep reduction in magnetisation on cooling from the highly magnetised austenitic phase to the nonmagnetic or anti-ferromagnetic martensitic phase. The peculiar magnetic property has led to a number of intriguing phenomena including an inverse magnetocaloric effect [23], a giant magnetoresistance effect [24], and a giant magnetothermal conductivity [25]. In particular, the Ni-Mn-In system with excess Mn exhibits the largest magnetocaloric effect and thus is regarded as a strong candidate in magnetic refrigeration applications without rare-earth elements [8]. In practice, an output stress exceeding 100 MPa arising from the MPT can be induced with this material, which is several ten times larger than that generated in Ni-Mn-Ga based FSMAs [7, 12, 22, 26].

To study the driving mechanism of this MPT, understanding of the underlying electronic structure is indispensable. For the related Ni-Mn-Sn alloys, where the excess Mn atoms occupy the vacant Sn sites, hard X-ray photoelectron spectroscopy (HAXPES) has been performed to explore the bulk electronic structure. The magnetic moment of the excess Mn at the Sn sites (denoted by  $\text{Mn}_{\text{Sn}}$  hereafter) is antiparallel to that of Mn at the ordinary sites. With 3d-orbital hybridisation occurring between  $\text{Mn}_{\text{Sn}}$  and Ni, the Ni 3d minority spin  $e_g$  state shifts towards the Fermi energy ( $E_{\text{F}}$ ) and splits into two levels above and below the Fermi energy, which stabilises the martensitic phase [27]. Whereas the  $\text{Mn}_{\text{Mn}}\text{-Mn}_{\text{Sn}}$  coupling of Ni-Mn-Sn is antiferromagnetic, the Ni-Mn-In system exhibits different magnetic properties because of its ferromagnetic  $\text{Mn}_{\text{Mn}}\text{-Mn}_{\text{In}}$  coupling [28–30], where  $\text{Mn}_{\text{Mn}}$  and  $\text{Mn}_{\text{In}}$  denote Mn atoms at ordinary and In sites, respectively. It is expected that such a difference in magnetic properties stems

from the electronic structure. To clarify the origin of the MPT and the related magnetic and electronic properties for  $\text{Ni}_2\text{Mn}_{1+x}\text{In}_{1-x}$  from the electronic structure point of view, HAXPES and first-principles calculation have been employed.

## 4.2 Experimental method

Polycrystalline  $\text{Ni}_2\text{Mn}_{1+x}\text{In}_{1-x}$  ( $x=0, 0.12, 0.24$  and  $0.36$ ) samples were prepared by a procedure described elsewhere [22, 28]. Using the standard Rietveld technique, structural refinement of the samples was performed from X-ray powder diffraction data. All the samples were shown to crystallise in the  $L2_1$  structure at room temperature. Furthermore, the excess Mn atoms in  $\text{Ni}_2\text{Mn}_{1+x}\text{In}_{1-x}$  ( $x=0, 0.12, 0.24$  and  $0.36$ ) were confirmed to occupy the vacant In sites. The HAXPES measurements were performed at BL15XU of SPring-8 [31, 32]. A photon energy of  $\sim 6$  keV was employed in the experiment with total energy resolution set to 240 meV. The binding energy ( $E_B$ ) was referred to the Fermi level of an evaporated Au film. The inelastic mean free path of 6 keV photoelectrons reaches about 5 nm, and hence the surface contribution to the photoelectron spectrum is well suppressed. All of the measurements were performed in an ultrahigh vacuum (better than  $2 \times 10^{-7}$  Pa). Contaminant-free sample surfaces were obtained by *in situ* fracturing. The calculations were performed with the Vienna ab initio simulation package [33, 34]. The spin-polarized generalized gradient approximation [35] was adopted for the exchange and correlation energies. The atomic core potential was described by the projector augmented wave method [36, 37]. To account for the effect of excess Mn atoms substituted at In sites in the band structures, the periodic supercells containing four formula units; i.e.  $\text{Ni}_8\text{Mn}_4\text{In}_4$ ,  $\text{Ni}_8\text{Mn}_5\text{In}_3$  and  $\text{Ni}_8\text{Mn}_6\text{In}_2$ , are assumed for  $x = 0, 0.25$  and  $0.5$ , respectively.

## 4.3 Results and discussion

Figure 17(a) shows the valence-band (VB) photoelectron spectra of  $\text{Ni}_2\text{Mn}_{1+x}\text{In}_{1-x}$  ( $x=0, 0.12, 0.24$  and  $0.36$ ) acquired at 250 K. The spectrum of the mother crystal ( $x=0$ ) shows five local intensity maxima around  $E_B$  of 0.2 eV (A), 1.4 eV (B), 2.4 eV (C), 4.6 eV (D), and 7.2 eV (E). Note that the peak A is found at smaller  $E_B$  by 0.2 eV than that of  $\text{Ni}_2\text{MnSn}$  [27]. This is consistent with the smaller valence electron concentration

( $e/a$ ) of  $\text{Ni}_2\text{MnIn}$  (7.5) than that of  $\text{Ni}_2\text{MnSn}$  (7.75) in the rigid band model. At first glance, the peak A is quite sharp for  $x=0-0.24$  exhibiting dips between the first and second peaks [12, 38], whereas this dip is less clear for  $x=0.36$ . Additionally, we see that the energy positions of this peak are the same for different  $x$  in sharp contrast to the result for  $\text{Ni}_2\text{Mn}_{1+x}\text{Sn}_{1-x}$ , where it shifts towards  $E_F$  with increasing  $x$  [27]. The intensity around  $E_B=6$  eV is slightly larger for  $x=0.36$  compared with those for lower Mn compositions.

The temperature variation [Fig. 17(b)] of the VB spectra for the  $x=0.36$  sample, which only exhibits the MPT in this temperature range, was measured while cooling the sample from 300 K to 150 K at intervals of 50 K. After reaching the lowest temperature (150 K), the sample was rewarmed to 250 K. The temperature dependence of the VB spectra for this sample shows that the peak near  $E_F$  at 250 K is persistent on cooling at least down to 200 K. However, the peak intensity is reduced considerably at 150 K [Fig. 17(b)], which is attributable to the MPT. Figure 17(c) shows a magnified view of the temperature-induced changes in the electronic state near  $E_F$  for the spectra taken at 150 K and 250 K. We note that the spectral weight near  $E_F$  at 250 K is transferred to the higher  $E_B$  side at 150 K, which results in a pseudogap formation at  $E_F$  in the martensitic phase. The observed pseudogap should be responsible for the prominent magnetoresistance [24].

To examine the changes in the electronic states during the MPT, we have performed temperature dependent VB measurements in detail. First, to find the transition temperature, the sample was cooled from 190 K to 70 K at 20 K intervals. As shown in Fig. 18(a), we confirmed that the MPT was completed at 70 K. The peak-and-dip feature near  $E_F$ , as an indicator of the austenitic phase, was found to diminish with decreasing temperature and no peak was recognisable when the MPT was completed. No noticeable change was found on cooling from 190 K (austenitic phase) to 150 K, and the spectrum acquired at 110 K resembled that of the martensitic phase at 70 K. Therefore we infer that the MPT starts at 150 K and finishes at 110 K. The temperature dependent spectra also imply the coexistence of the martensitic and austenitic phases in the sample at 130 K. Note that the transition temperature shown in Fig. 18(a) is slightly lower than that

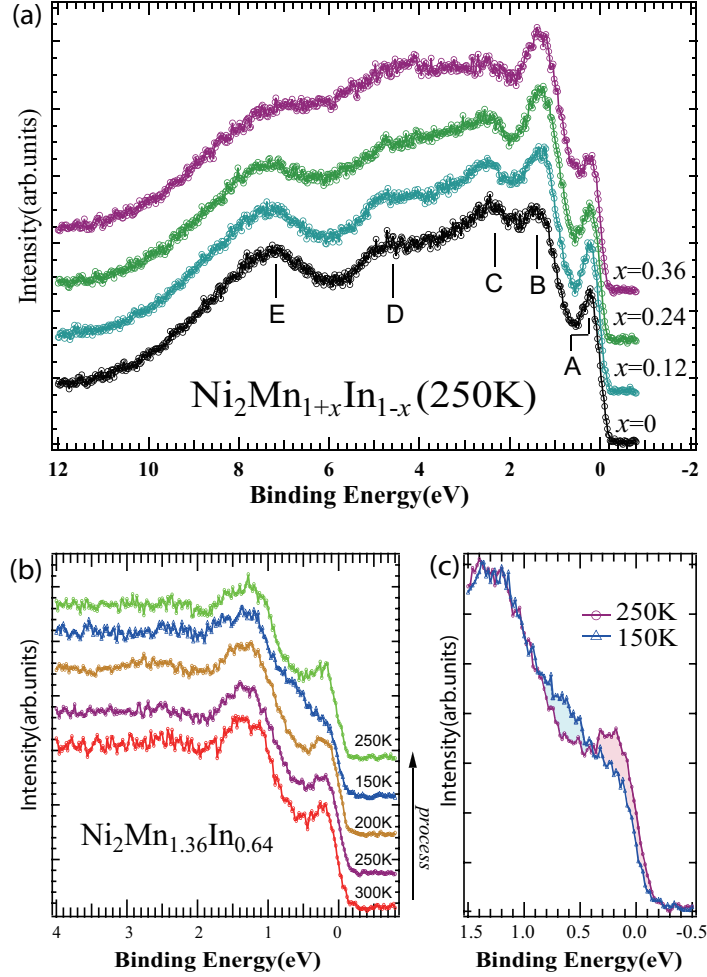


Figure 17: (Color online) (a) Photoelectron spectra of  $\text{Ni}_2\text{Mn}_{1+x}\text{In}_{1-x}$  ( $x=0, 0.12, 0.24$  and  $0.36$ ) measured at 250 K. ( $h\nu=5953.4$  eV) The binding energy is referred to the Fermi energy. Five peaks located at the binding energies of 0.2 eV, 1.4 eV, 2.4 eV, 4.6 eV and 7.2 eV are marked as A, B, C, D and E, respectively. (b) Valence-band spectra of  $\text{Ni}_2\text{Mn}_{1+x}\text{In}_{1-x}$  ( $x=0.36$ ) measured on cooling from 300 K to 150 K at temperature intervals of 50 K, and finally taken at the elevated temperature of 250 K. (c) Magnified view of the spectra taken at 150 K and 250 K near the Fermi energy.

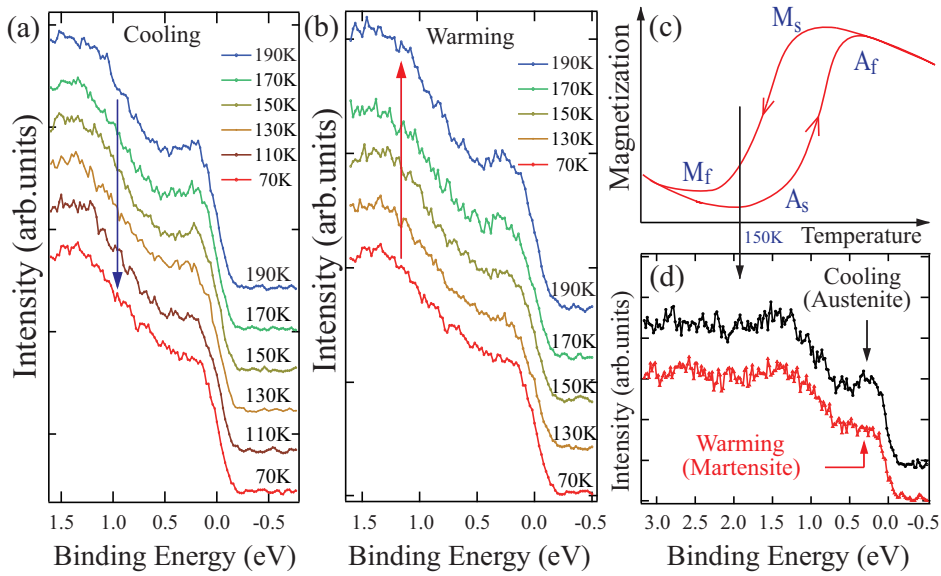


Figure 18: (Color online) Photoelectron spectra of  $\text{Ni}_2\text{Mn}_{1+x}\text{In}_{1-x}$  ( $x=0.36$ ) measured (a) on cooling and (b) on warming. (c) Schematic diagram of the temperature dependent magnetisation. (d) Comparison of the spectra measured at 150 K on cooling (black) and warming (red).

in the separate measurement of Fig. 17(b), because the transition is quite sensitive to stoichiometry (in particular Mn concentration), which may depend on cleavage planes. Figure 18(b) shows the VB spectra acquired from 70 K to 190 K at 20 K intervals. We found that the MPT starts at 130 K and finishes at 170 K. By comparing the results on warming with those on cooling, a hysteretic behaviour was clearly observed in the electronic structure near  $E_F$ . These results are consistent with the temperature dependent magnetization curve as schematically shown in Fig. 18(c) [22].

To assess the reproducibility of these results, we rewarmed the sample to room temperature and reset the sample for more than 1 day before cooling again to 150 K. After the measurement of VB spectrum in a short  $E_B$  range at 150 K as indicated by red line in Fig. 18(d), the sample was cooled to 70 K and then rewarmed to 150 K. We measured again the VB spectrum in the short  $E_B$  range at 150 K as indicated by black line in Fig. 18(d). One sees that the peak-and-dip feature near  $E_F$  appears only on cooling at 150 K, whereas it is absent on warming, again confirming hysteretic behaviour of the electronic states.

To explain the role of the excess Mn atoms in the MPT for the Ni-Mn-In alloys, we

have performed first-principles density-functional calculations. As seen in Fig. 19(a), for stoichiometric Ni<sub>2</sub>MnIn, a sharp minority-spin density of states (DOS) mainly with Ni 3d  $e_g$  character is found at 0.2 eV, whereas the majority spin DOS is small and featureless near  $E_F$ . The energy position of Ni 3d minority spin state for Ni<sub>2</sub>MnIn located at  $E_B=0.2$  eV is lower than that for Ni<sub>2</sub>MnSn [27]. This difference is consistent with our experimental result [see Fig. 17(a) in this work and Fig. 18(a) in Ref.[13]]. Let us now consider the evolution of the DOS against the excess Mn atoms substituted at the In sites. As seen in Fig. 19(a), a minor peak feature appears at  $E_B=0.1$  eV in addition to the main peak at 0.2 eV for  $x=0.25$  in the minority spin state. This minor peak feature near  $E_F$  for  $x=0.25$  shifts toward lower  $E_B$  side and eventually the DOS has a peak at  $E_F$  for  $x=0.5$  upon the excess Mn substitution, which would lead to an instability in the austenitic phase. In contrast, the main peak around 0.2 eV is quite persistent and does not move significantly from  $x=0.25$  to 0.5. We recall that experimentally no energy shift of the peak at 0.2 eV for different  $x$  is found. We speculate here that due to the experimental resolution the minor peak in the theoretical Ni 3d  $e_g$  minority-spin DOS has not been experimentally resolved. In the tetragonal phase ( $c/a=1.17$ ), the dominant DOS above 0.5 eV and the small structureless DOS below 0.5 eV are seen for both the majority and minority spin states. Figure 19(b) shows the calculated Ni 3d  $e_g$  partial DOS in the FM cubic phase for  $x=0.5$ . Also Ni 3d<sub>3z<sup>2</sup>-r<sup>2</sup></sub> and 3d<sub>x<sup>2</sup>-y<sup>2</sup></sub> components are shown for the AFM tetragonal phase. Here, the states with antiparallel and parallel couplings between Mn<sub>Mn</sub> and Mn<sub>In</sub> spins are labeled as AFM and FM, respectively [see the schematic illustration of crystal structures in Figs 19(c) and 19(d)]. In the cubic phase, the minority-spin Ni 3d  $e_g$  state crosses  $E_F$ , with 3d<sub>x<sup>2</sup>-y<sup>2</sup></sub> and 3d<sub>3z<sup>2</sup>-r<sup>2</sup></sub> degenerated. In the AFM tetragonal phase, however, the two orbital components are not degenerate anymore due to the lower symmetry. By the interaction of Ni atom with the neighbour atoms in the  $x$ - $y$  plane, the minority-spin 3d<sub>x<sup>2</sup>-y<sup>2</sup></sub> splits into bonding and anti-bonding states, while the minority-spin 3d<sub>3z<sup>2</sup>-r<sup>2</sup></sub> shifts to lower energy. As a result of the splitting in the the minority-spin 3d<sub>x<sup>2</sup>-y<sup>2</sup></sub> state, a pseudo gap is formed at  $E_F$ . This is consistent with the experimental result.

As shown in Fig. 20(a), the total-energy variation, which is caused by the tetragonal

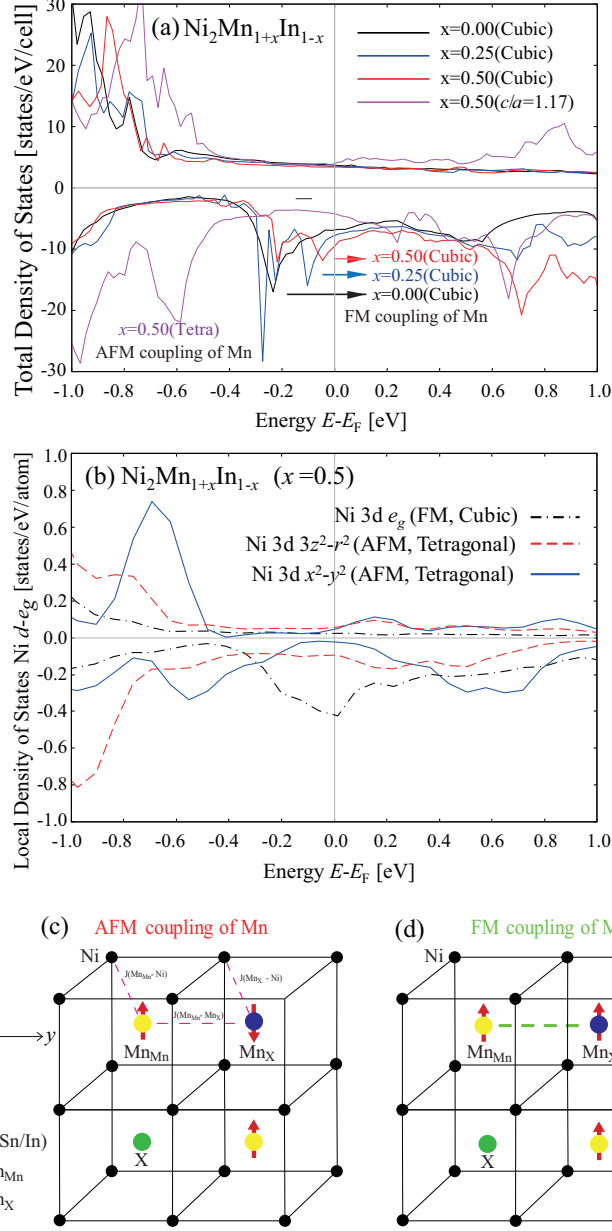


Figure 19: (Color online) (a) Calculated total density of states (DOSs) near  $E_F$ , in the cubic (austenitic) phase of  $\text{Ni}_2\text{Mn}_{1+x}\text{In}_{1-x}$  for  $x=0, 0.25$ , and  $0.5$ , respectively. The DOS in the tetragonal phase ( $c/a=1.17$ ) for  $x=0.5$  is also shown for comparison. (b) Calculated Ni  $3d e_g$  partial DOS in the FM cubic phase for  $x=0.5$ . Also Ni  $3d 3z^2-r^2$  and  $3d x^2-y^2$  components are shown for the AFM tetragonal phase. (c) and (d) schematically show AFM and FM coupling of Mn spins, respectively.



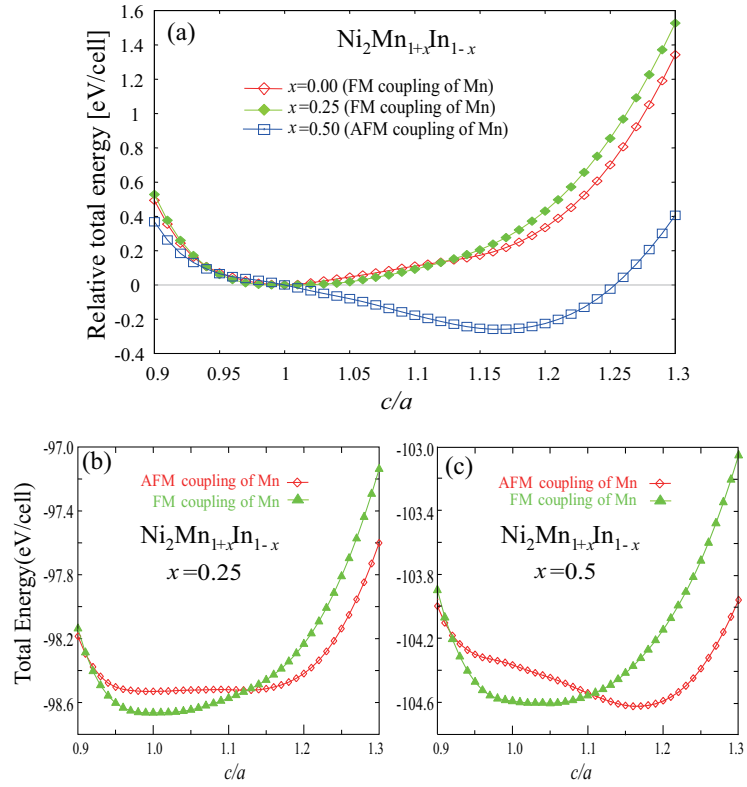


Figure 20: (Color online) (a) Total energy difference (per formula unit) relative to the cubic phase as a function of the axial ratio,  $c/a$ , in the tetragonal structure calculated for  $\text{Ni}_2\text{Mn}_{1+x}\text{In}_{1-x}$  ( $x=0, 0.25$ , and  $0.5$ ). (b) and (c) show the FM and AFM coupling between  $\text{Mn}_{\text{Mn}}\text{-Mn}_{\text{In}}$  sites for  $x=0.25$  and  $0.5$ , respectively.

distortion from the cubic phase has been calculated with a fixed cell volume for  $\text{Ni}_2\text{Mn}_{1+x}\text{In}_{1-x}$ . We found that the cubic cell is the most stable for  $x=0$  and  $0.25$ . In contrast, for  $x=0.5$ , the tetragonal cell with  $c/a=1.17$  takes its global energy minimum instead of the cubic cell. Fig. 20(b) shows that for  $x=0.25$  the total energy of the state with FM coupling has a minimum at  $c/a=1$ , whereas two minima appear around  $c/a=1$  and  $1.17$  for AFM coupling. As the minimum energy for FM coupling is lower than that for AFM coupling, the  $\text{Mn}_{\text{Mn}}\text{-Mn}_{\text{In}}$  spin coupling for  $x=0.25$  is predicted to be ferromagnetic. In Fig. 20(c), the state with FM coupling for  $x=0.5$  has a minimum at  $c/a=1$ , whereas the state with AFM coupling is lowest in energy at  $c/a=1.17$ . Hence antiparallel  $\text{Mn}_{\text{Mn}}\text{-Mn}_{\text{In}}$  spin coupling is expected for  $x=0.5$ . From these results we establish that the MPT in the composition range of  $x=0.25\text{--}0.5$  is accompanied by a competition of the FM and AFM couplings between the spins in the  $\text{Mn}_{\text{Mn}}\text{-Mn}_{\text{In}}$  sites. This situation is different to that for the  $\text{NiMnSn}$  system, where the AFM coupling between the spins in the  $\text{Mn}_{\text{Mn}}\text{-Mn}_{\text{Sn}}$  sites has been predicted for both austenitic and martensitic phases [27]. It has been recently shown that the energy minimum of the state with FM  $\text{Mn}_{\text{Mn}}\text{-Mn}_{\text{In}}$  spin coupling can be much lower than that with AFM coupling for  $\text{Ni}_{1.75}\text{Co}_{0.25}\text{Mn}_{1.5}\text{In}_{0.5}$ , where a portion of Ni sites are replaced with Co. It is in strong contrast to the present work as demonstrated in Figs 20(c). This again confirms that the Ni and/or Co 3d states would be a key factor to determine the  $\text{Mn}_{\text{Mn}}\text{-Mn}_{\text{In}}$  spin coupling manner [39].

#### 4.4 Conclusion

In summary, the electronic structures of  $\text{Ni}_2\text{Mn}_{1+x}\text{In}_{1-x}$  have been explored by means of bulk sensitive hard-X-ray photoelectron spectroscopy and first-principles density-functional calculations. A substantial temperature-induced change as well as hysteretic behaviour have been clearly observed for the minority-spin Ni 3d  $e_g$  state located just below  $E_F$ , signifying a strong relationship of this state with martensitic phase transition. Importantly, we found that the spectral weight near  $E_F$  is reduced considerably and is transferred to higher  $E_B$ , resulting in a pseudogap formation in the martensitic phase. Thus we conclude this pseudogap formation is the origin of higher resistivity and hence the prominent magnetoresistance. Both experimental and theoretical studies

have revealed that the the minority-spin Ni 3d  $e_g$  state plays an important role in stabilizing the martensitic phase in the presence of excess Mn. The first-principles calculation has shown that the anti-ferromagnetic  $\text{Mn}_{\text{Mn}}\text{-Mn}_{\text{In}}$  spin coupling is preferred in the martensitic phase for  $\text{Ni}_2\text{Mn}_{1.5}\text{In}_{0.5}$ . Such a spin-coupling manner originates from the minority-spin Ni 3d  $e_g$  state as a key ingredient of structural instability.

# 5 Ultrafast electron dynamics at the Dirac node of the topological insulator $\text{Sb}_2\text{Te}_3$

## 5.1 Introduction

Angle resolved photoemission spectroscopy (ARPES) implemented by a pump-and-probe method is a powerful tool to study the unoccupied states and electron dynamics with energy and momentum resolutions. Many groups have made great progresses on topological insulators with the time-resolved ARPES. [57–68]. Recently, owing to a rather high energy resolution (sub-20meV) derived from a Ti:sapphire laser system, we have the chance to optically observe electron dynamics of the fine structures near Dirac node[69]. To unveil the electron decay process below and above the Dirac node, we need an initial state situation (for example, before pumping) in which both the upper and lower parts of the Dirac cone are empty. This could be realized with *p*-type TIs, where the Dirac node is located above the Fermi energy,  $E_F$ . Graphene, whose Dirac node is almost at or below  $E_F$ , is therefore not suitable for this purpose. The *p*-type  $\text{Bi}_2\text{Se}_3$  is also unsuitable because the lower part of Dirac cone is not energetically isolated from the bulk valence band [70]. This feature can also be seen from the absence of the Landau level quantization in the lower part of the surface Dirac cone, while it is visible above the Dirac node [72, 73]. In contrast,  $\text{Sb}_2\text{Te}_3$  shows surface Landau quantizations over the energy range of  $\sim 240$  meV (120 meV below and 120 meV above the Dirac node) [74, 75]. Here, the Dirac cone SS is separated from the bulk states, which enables us to study an isolated Dirac cone. Second, a  $\text{Sb}_2\text{Te}_3$  single crystal is naturally *p*-doped, and the Dirac node is located above the  $E_F$ . Therefore, we do not need to dope any element into the mother crystal. This is advantageous when attempting to increase the quality of the sample. Having considered the abovementioned characteristics,  $\text{Sb}_2\text{Te}_3$  is suitable for the present study. In this study, we investigated the unoccupied bulk and surface states of  $\text{Sb}_2\text{Te}_3$  using time resolved ARPES (TrARPES). The electron dynamics below and above the Dirac node were also revealed. One of the most striking findings is that the decay of the pump-induced carriers are bottlenecked at the Dirac node, so that the hot carriers in the upper part of the SS stay longer than those in the lower part.

## 5.2 Experimental method

The  $\text{Sb}_2\text{Te}_3$  single crystal was grown by the Bridgeman method. The results of electron probe micro analysis (EPMA) showed an atomic ratio of  $\text{Sb}:\text{Te} = 2.03 : 2.97$ . The experiment was performed with linearly polarized 5.98 eV (probe) and 1.5 eV (pump) pulses derived from a Ti:sapphire laser system operating at a repetition rate of 250 kHz [69]. The photoelectron kinetic energy and emission angle were resolved using a hemispherical electron analyser. The measurement was done at 8 K with an energy resolution of  $\sim 15$  meV. The origin of the pump-and-probe delay ( $t = 0$ ) and the time resolution of 250 fs was determined from the TrARPES signal of graphite attached next to the sample. The spot diameters of the pump and probe were 0.5 and 0.3 mm, respectively.

## 5.3 Results and discussion

### 5.3.1 Experimental results

By pumping the electrons into the unoccupied side, we observed a linear Dirac cone SS as shown in Fig. 21(a). Here, the pump-and-probe delay,  $t$ , was set to 0.4 ps. The Dirac node is located  $\sim 180$  meV above the  $E_F$  and the Dirac velocity was estimated to be  $\sim 2.3 \times 10^5$  m/s. We found that both the upper and lower parts of the Dirac cone (UDC and LDC, respectively) were clearly visible above  $E_F$  and they do not overlap with the bulk continuum states. Figure. 21(b) shows the constant energy contours at 100, 290 and 410 meV. With increasing the energy, the SS evolves from a circular to hexagonal shape. The isotropic constant surface can be observed both below and above the Dirac node within the bulk energy gap. The hexagonal warping of the constant energy surfaces is quite small as long as no bulk continuum state overlaps with the SS. In the previous STM study on  $\text{Sb}_2\text{Te}_3$ , the Dirac node is 80 meV higher, whereas the energy range of the SS ( $\sim 120$  meV above and below the Dirac node) is consistent with the present observations [74, 75]. With such an ideal situation, there is a good opportunity to study the carrier dynamics of UDC and LDC separately, where interference from the bulk states is minimized.

To study the pump-induced dynamics of the surface Dirac fermions, we altered the

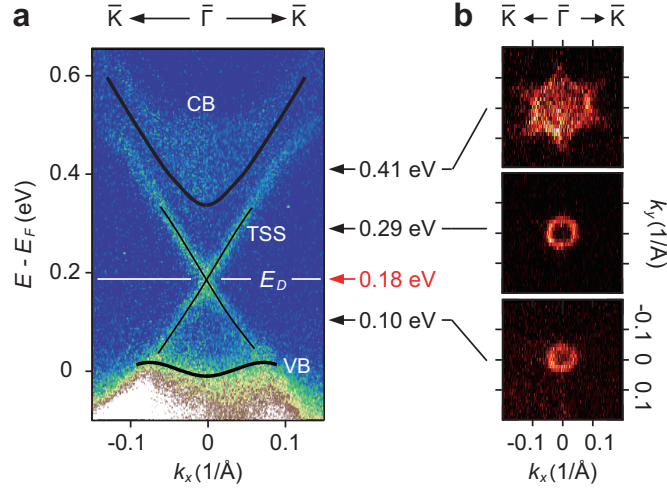


Figure 21: The electronic structure of  $\text{Sb}_2\text{Te}_3$ . (a) The TrARPES images of  $\text{Sb}_2\text{Te}_3$  along the  $\bar{\Gamma} - \bar{K}$  direction. (b) Constant energy maps at a binding energy of 100, 290 and 410 meV. The surface state evolves from a hexagonal to a circular shape.

pump and probe delay and investigated the time dependent variations in the TrARPES images. Figure 22(a) shows the difference image along the  $\bar{\Gamma} - \bar{K}$  line measured at  $t = 0.4$  ps. Both the Dirac cone SS and unoccupied bulk state were clearly observed. Here we notice that the dynamics of bulk and surface states are the same and only depend on the energy. As shown in Fig. 23, we altered the pump and probe delay and investigated the time dependent variations in the TrARPES images. Fig. 23(a) shows the difference image along the  $\bar{\Gamma} - \bar{K}$  line measured at  $t = 0.26$  ps. Here we clarified the bulk conduction band and two branches of UDC as Bulk, Surface\_ A and Surface\_ B, respectively. We set energy and momentum frames and plotted the normalized intensity variation in each frame as functions of  $t$  [see Fig. 23(b)-(i)]. The intensities in a same energy range are normalized. The intensity variations of bulk and surface states do not show significantly difference. That means the electron dynamics only depend on the energy. To show the energy dependent dynamics, we set energy and momentum frames [A to I: see Fig. 22(a)] and plotted the intensity variation in each frame as functions of  $t$  [see Fig. 22(b)]. Also, to show the variation in the different bands more clearly, we show the original and difference images for typical delay times [see Fig. 22(v)].

In the highest energy region A, we observed a fast rise of intensity that was limited by the time resolution without any significant delay. The intensity variation was almost symmetric about  $t = 0$ . This indicates that the intensity variation in region A comprises

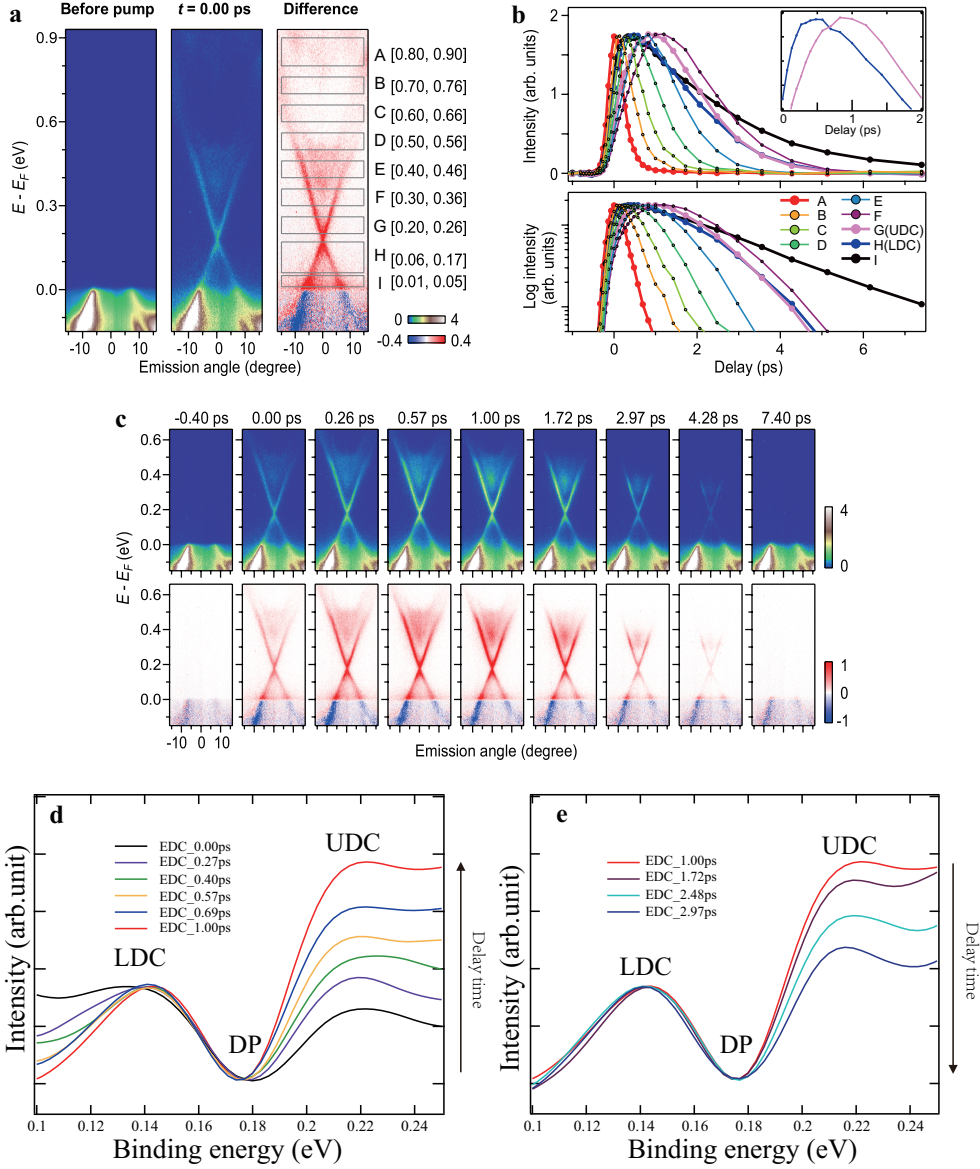


Figure 22: The time dependent study of  $\text{Sb}_2\text{Te}_3$  spectra. (a) The  $\text{Sb}_2\text{Te}_3$  spectra along the  $\bar{\Gamma} - \bar{K}$  line measured at  $t = -0.4$  ps,  $t = 0.4$  ps and the difference image at  $t = 0.4$  ps. The energy ranges 0.8-0.9eV, 0.7-0.76 eV, 0.6-0.66 eV, 0.5-0.56 eV, 0.4-0.46 eV, 0.3-0.36 eV, 0.2-0.26 eV, 0.06-0.17 eV and 0.01-0.05 eV are marked as A, B, C, D, E, F, G, H and I, respectively. (b) The decay behaviour of different energy ranges indicated in (a) described using the normalized intensity and their common logarithms. Inset panel shows the intensity variation lines of region G and H. (c) The spectra were measured with delay times of  $t = -0.4$  ps,  $0$  ps,  $0.26$  ps,  $0.57$  ps,  $1.00$  ps,  $1.72$  ps,  $2.97$  ps,  $4.28$  ps and  $7.40$  ps, respectively. The lower parts are the difference spectra. (d) EDC spectra at  $t = 0$  ps,  $0.27$  ps,  $0.4$  ps,  $0.57$  ps,  $0.69$  ps and  $1$  ps. (e) EDC spectra at  $t = 1$  ps,  $1.72$  ps,  $2.48$  ps and  $2.97$  ps. Intensity of EDCs are normalized by the peak intensity of LDC.

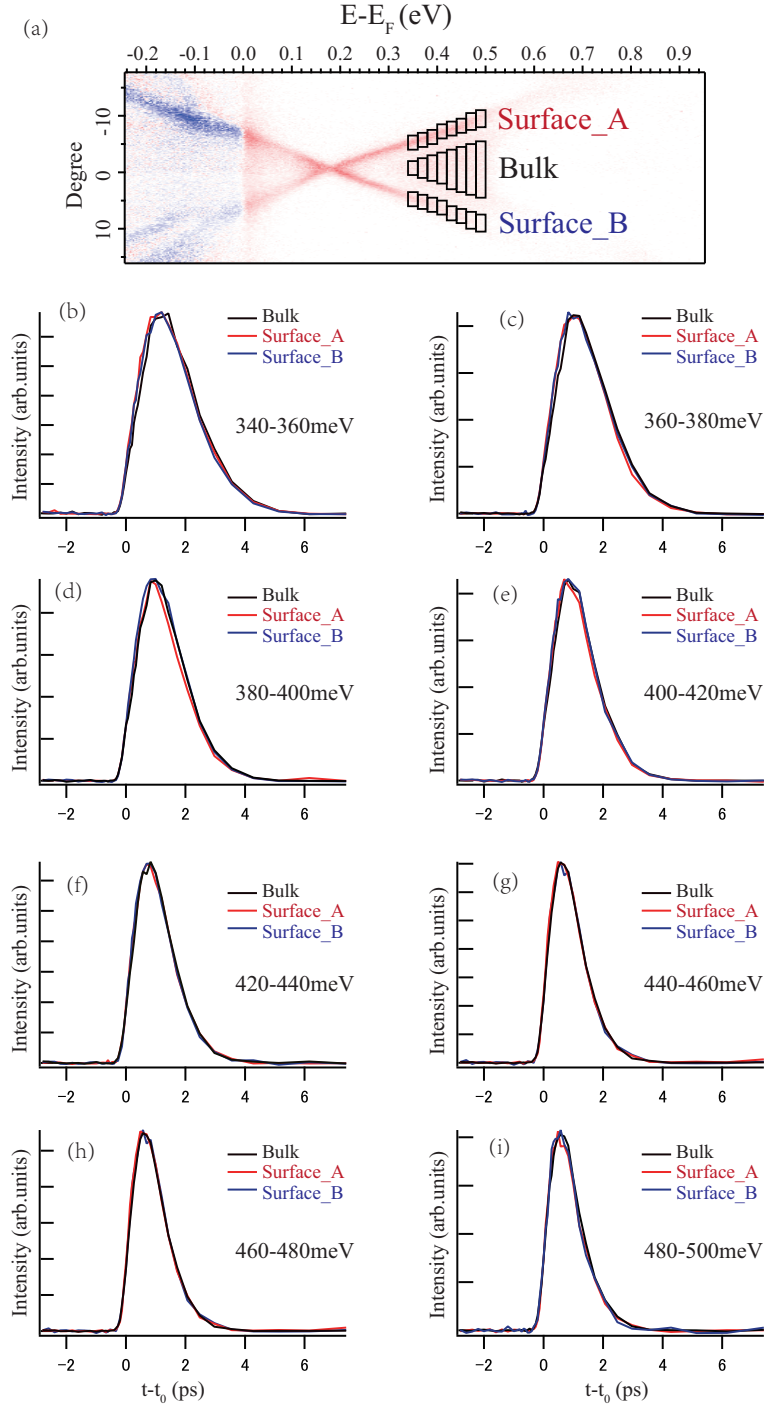


Figure 23: Decay behaviors of bulk and surface states (a) The difference image at  $t = 0.26$  ps. The bulk conduction band and two branches of UDC are marked as Bulk, Surface\_A and Surface\_B, respectively. (b)-(i) The decay behaviour of Bulk, Surface\_A and Surface\_B at different energy ranges (340-360 meV, 360-380 meV, 380-400 meV, 400-420 meV, 420-440 meV, 440-460 meV, 460-480 meV and 480-500 meV).



instantaneous filling of the states by direct excitations and very fast flow of the excited electrons out of region A into the lower energy states. Because the flow of electrons into region A from higher energies is negligibly small, the line shape does not show significant asymmetric tailing into  $t > 0$ .

Next, we investigated the higher energy regions A, B, C, D, E and F, which are in the conduction band. It was observed that the duration of the intensity variation became long as the Dirac node was approached. This indicates that there was an energy dependence on the flow rate of electrons. The net flow rate of electrons from high to low energy decreased when the Dirac point was approached. This can occur because the available phase space diminishes on the approach of the Dirac node, and so the hot carriers pile up around the bottom of the UDC. Similar behaviour was observed above the Dirac node for  $\text{Bi}_2\text{Se}_3$  [59]. Considering that the behaviour can be represented by an exponential decay, the decay constant,  $\tau$ , of the different regions varied from 0.2 ps to 2 ps, which is comparable to a recent study on  $\text{Sb}_2\text{Te}_3$  [76].

The most striking observation was found across the Dirac node, namely in the intensity variations between regions G and H. Although region H in the LDC was located lower than G in the UDC, the duration of the intensity variation in H was much faster than that in G and was even faster than that in region D [see Fig. 22(b,c)]. Seeing the intensity variation line profiles of regions G and H, two crossing points can be found at  $\sim 0.6$  ps and  $\sim 3.5$  ps. It shows that a population inversion takes place in the time domain of 0.6-3.5 ps as depicted in the inset of Fig. 22(b). To demonstrate the population inversion more clearly, we show the energy distribution curves (EDCs) measured at different delay times in Fig. 22(d,e). We can find that compared with intensity of LDC, the intensity of UDC normalized with respect to that of LDC increases before 1 ps and decreases after 1 ps, as shown in Fig. 22(d) and Fig. 22(e).

Viewing the whole decay process [see Fig. 22(c) and supplementary movie S4], the node acts as a bottleneck in the net flow of particles into the lower cone and therefore a population inversion occurs near the node. Here we note that the low DOS near Dirac node plays a key role in the observed population inversion. To prove this idea, we have made two simulations. The first simulation shows the decay behavior

induced by the thermal distribution and we find that the population inversion can not be produced simply by thermal distribution [see supplementary Fig. S2 online]. The second simulation demonstrates the time evolution of the intensity variation lines with and without the low DOS region. We find that the population inversion can be explained only when the relatively small DOS region, like Dirac node, is considered [see supplementary Fig. S3 online]. The double crossing points correspond to the onset and the final points of ‘electron jam’ near the Dirac node, which is qualitatively reproduced in the simulation.

We also observed that the intensity variation in region I, which is close to the Fermi level, showed the third fastest response after regions A and B. The ultrafast response of the low energy excitations around the Fermi level was attributed to the impact ionization, in which the low energy excitations at the Fermi level is accompanied by direct excitation because of the orthogonal catastrophe [77–79]. The spectral changes because of the impact ionization are limited below 50 meV and appear to be similar to the broadening of the Fermi cutoff after pumping, as observed in time resolved photoemission studies on metals [80]. Because the effect of impact ionization occurs only in the vicinity of the Fermi level, the carrier dynamics within the SS are less affected by the impact ionization.

Schematics of the pump and decay processes from the original state before pumping [Fig. 24(a)] to the final state [Fig. 24(e)] are shown in Fig. 24. As shown in Fig. 24(b), the electrons are directly excited from the occupied states, with impact ionization. As shown in Fig. 24(c), one may imagine that the electrons in the upper states simply drop into the lower energy states. In reality, however, things are more complicated. Because of the low density of states, there is a bottleneck to the drop near the Dirac node. This effect leads to the hourglass shape shown in Fig. 24(d).

### 5.3.2 simulation

#### I Simulation of decay behavior from thermal distribution

To distinguish from the hourglass effect, we simulate the decay behavior caused by thermal distribution. First of all, we simulate the Fermi Dirac distribution with absolute temperature  $T = T_0$ , as shown in the inset panel of Fig. 25. Then

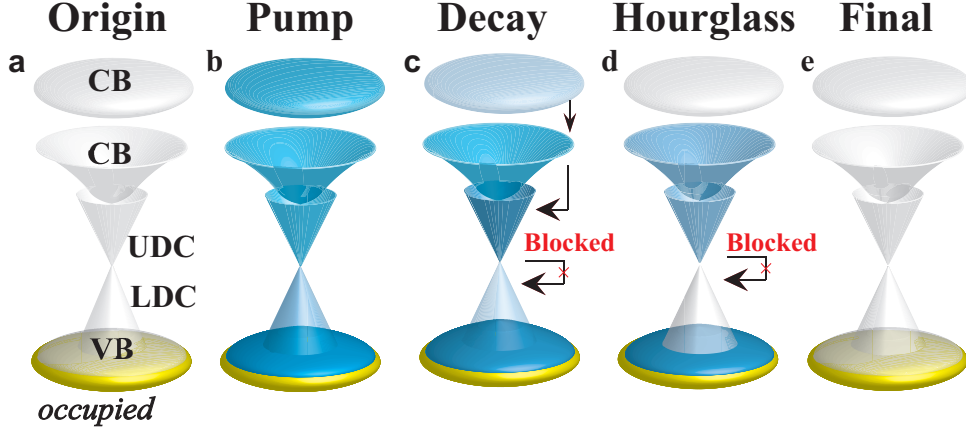


Figure 24: The schematic figures of the pump and decay processes. The schematic of the pump and decay processes discussed in this report, including (a) the original state, (b) the pumping behaviour and (c) the decaying behaviour of the states, which leads to (d) the hourglass shape. The final state is shown in (e). The deeper colour indicates there is a higher electron intensity.

we assumed that during the decay process temperature  $T$  decays as  $T = T_1 + (T_0 - T_1) * \exp(-t/\tau)$ , where  $T_0$  is the initial temperature,  $T_1$  is the final temperature,  $\tau$  is the relaxation time and  $t$  is the time. Here we alerted five binding energies  $E1, E2, E3, E4$  and  $E5$ (marked in the inset panel) and simulated the decay behaviors at these energies, as shown in Fig. 25. We could find that the electrons at higher energy always shows faster decay. From this result we can conclude that the origin of hourglass effect is not the thermal distribution.

## II Simulation of hourglass effect

To quantitatively prove the origin of hourglass effect, we simulated the decay lines with and without low DOS region. Here we consider a simple model with 10 energy regions, marked as S0-S9. The binding energy of region S9 is the highest and S0 is the lowest. Intensity of S0 was assumed only from direct excitation. Only the decays from neighbor regions were taken into account. The intensity of region S9 was considered to follow an exponential decay.

Considering a uniform DOS, as shown in the upper panel of Fig. 26 (c), we can simulate the decay lines of different energy regions. As shown in Fig. 26 (a), high binding energy region always shows earlier rising edge Therefore hourglass effect can

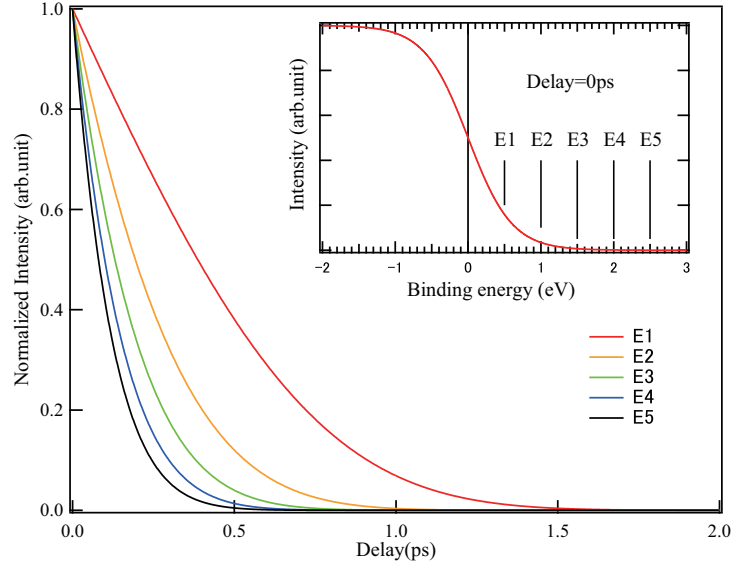


Figure 25: Simulation of decay behavior from thermal distribution (a) The TrARPES images of  $\text{Sb}_2\text{Te}_3$  along the  $\bar{\Gamma} - \bar{K}$  direction. (b) Constant energy maps at a binding energy of 100, 290 and 410 meV. The surface state evolves from a hexagonal to a circular shape.

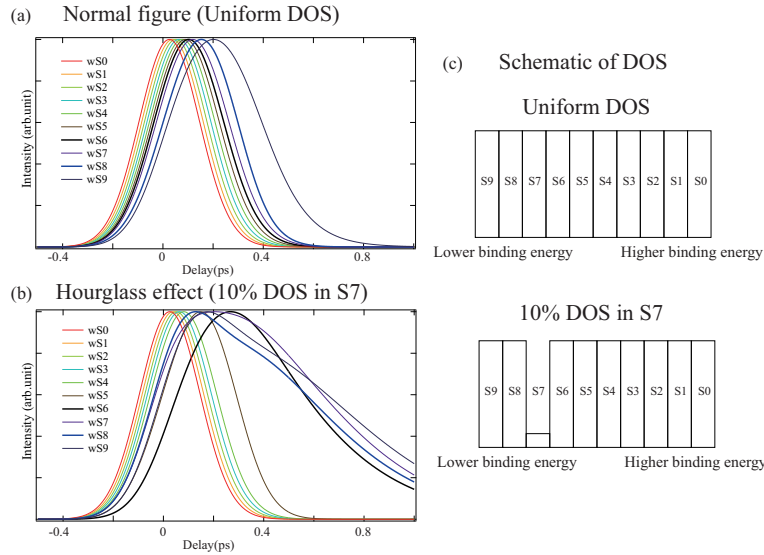


Figure 26: Simulation of a simple model for hourglass effect (a) Simulated decay lines assuming a uniform DOS distribution. (b) Simulated decay lines assuming 10% DOS at energy region S7. (c) Schematic figures for the assumed DOS distributions in the simulation.

not be realized with a uniform DOS.

While we decreased the DOS of region S7 to 10%, as shown in the lower panel of Fig. 26 (c), we made the simulation again without changing any other parameters. As shown in Fig. 26 (b), a big change occurred for the regions lower than S6, while the higher energy regions do not change significantly. Intensity peak of region S8 shifted to much earlier delay time than region S6, just like what we experimentally observed for UDC and LDC. This result can be a powerful improvement assisting that the hourglass effect was induced by the low DOS near Dirac node.

## 5.4 Conclusion

The conclusion is three-fold. First, TrARPES on  $\text{Sb}_2\text{Te}_3$  revealed the surface state Dirac cone in the unoccupied region. It was found to be isotropic within the bulk energy gap and the Dirac velocity was larger than that of  $\text{Bi}_2\text{Se}_3$ . Second, a rapid intensity increase was found near  $E_F$ , which was caused by the creation of a large number of low energy electron–hole pairs. Third, we found that the intensity in the upper part of the Dirac cone decreased much more slowly than below the Dirac node because of the absence of the density of states at the Dirac node. The population inversion in the Dirac dispersion may be used as an optical gain medium for broad band lasing if the duration of the inversion can be elongated [81], for example, by continuously injecting carriers into the UDC.

# 6 X-ray magnetic circular dichroism study of ferromagnetic topological insulator V-doped $\text{Sb}_2\text{Te}_3$

## 6.1 Introduction

Topological insulators (TIs) with a massless Dirac cone edge or surface state protected by time-reversal symmetry is one of the hottest topics since discovered [82]. This characteristic is directly related to a weak antilocalization of the Dirac fermions [83]. Breaking the time-reversal symmetry in the TIs is predicted to create a variety of exotic topological phenomena including the half-quantized Hall conductance, image magnetic monopoles, giant magneto-optical effects, and quantized anomalous Hall effect [15]. Recently, quantized anomalous Hall effect is realized with Cr-doped system. However, the low Curie temperature ( $\sim 15\text{K}$ ) limits the application. Even though there are many ferromagnetic TIs reported previously, including  $\text{Bi}_2\text{Te}_3$ ,  $\text{Bi}_2\text{Se}_3$  and  $\text{Sb}_2\text{Te}_3$  systems, possible choices are limited. For  $\text{Bi}_2\text{Te}_3$ , the Dirac cone locates in the energy range of bulk valence band [82]. For Mn-doped  $\text{Bi}_2\text{Se}_3$ , the Curie temperature is high and calculated band dispersion shows ideal Dirac cone [71, 82]. However, recent STM experiment shows that Landau levels below DP are missing, which means the surface state (SS) below Dirac point (DP) is covered by the bulk valence band [72, 73]. For  $\text{Sb}_2\text{Te}_3$ , the Landau Level appears not only above but also below the DP [74, 75]. Therefore,  $\text{Sb}_2\text{Te}_3$  is a good candidate to host QAH effect. To raise the Curie temperature, driving mechanism of ferromagnetism is necessary to be scrutinized. In this paper, we employed XMCD to study the element specific magnetic moment, and proved the mechanism in V-doped  $\text{Sb}_2\text{Te}_3$  to be carrier mediated. Searching for these novel phenomena in magnetically doped TIs represents one of the most exciting areas in this field. The superconducting quantum interference device (SQUID) is very useful, but it should be notable that not only the doped elements contribute to the magnetism. With the X-ray magnetic circular dichroism (XMCD), elemental specific magnetic moments can be evaluated [84].

In our experiment, we have observed XMCD spectra at V  $L_{23}$  edge, Sb  $M_{45}$  edge and Te  $M_{45}$  edge at  $\pm 8\text{T}$ ,  $5\text{K}$ . The helicity of the circular polarization was switched

periodically (1Hz), using a kicker magnet system. From XAS, we can clearly observe the absorption edges of V  $2p$ , Sb  $3d$  and Te  $3d$  states. According to XMCD result, even though V shows the magnetic moments, both Sb and Te show visible magnetic moments. With M-H measurement, the hysteresis behavior at V  $L_3$  edge shows the ferromagnetism of V atoms. Interestingly, both Sb and Te  $M_5$  edges show similar hysteresis behavior, which indicates that, the ferromagnetism of Sb and Te atoms are induced by doped V atoms. To study the magnetic anisotropy, we tilted the sample with 45 degree, and observed the variations of hysteresis behavior at V  $L_3$  and Sb  $M_5$  edges. With the magnetic coercivity decreases to  $\sim 50\%$ , we can conclude that the easy axis is out of plane.

## 6.2 Experimental method

The V-doped  $\text{Sb}_2\text{Te}_3$  single crystal was grown by the Bridgeman method. The results of electron probe micro analysis (EPMA) showed an atomic ratio of V:Sb:Te = 0.018 : 1.983: 2.998. To study the element specific magnetic moment, XMCD measurements was performed at the state-of-the-art twin helical undulator beamline BL23SU of SPring-8 with magnetic field up to 8T. The spectra were taken at 5K. The brilliant synchrotron light from an 8 GeV storage ring and the fast switching between left- and right-circular polarizations enabled the data acquisition with an appropriate signal-to-noise ratio. The samples were cleaved in-situ in an ultrahigh vacuum (better than  $5 \times 10^{-8}$  Pa) at room temperature, and then transferred to the liquid helium-cooled manipulator in the measurement chamber (better than  $5 \times 10^{-9}$  Pa) equipped with a super-conducting magnet. The XAS and XMCD spectra were acquired in a total electron yield mode. The trARPES experiment was performed with linearly polarized 5.98 eV (probe) and 1.5 eV (pump) pulses derived from a Ti:sapphire laser system operating at a repetition rate of 250 kHz. The photoelectron kinetic energy and emission angle were resolved using a hemispherical electron analyser. The measurement was done at 8 K with an energy resolution of  $\sim 15$  meV. The origin of the pump-and-probe delay ( $t = 0$ ) and the time resolution of 250 fs was determined from the tr-ARPES signal of graphite attached next to the sample. The spot diameters of the pump and probe were 0.5 and 0.3 mm, respectively [69].

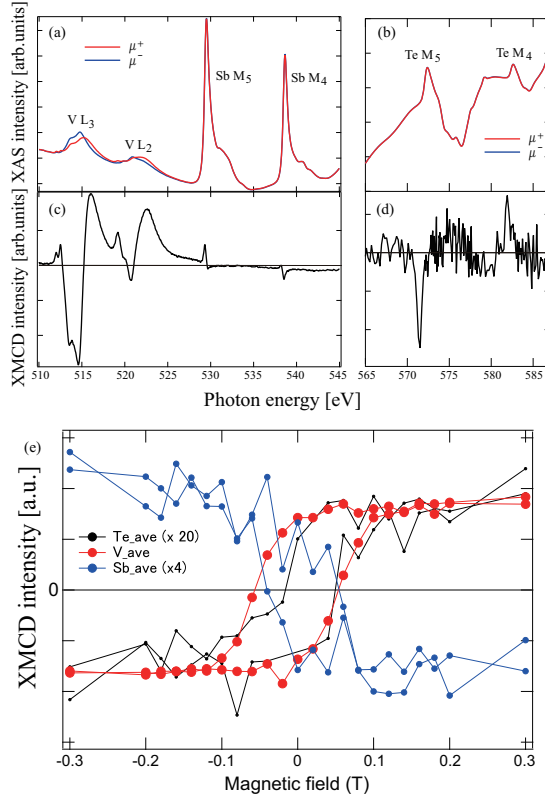


Figure 27: Element specific magnetic moment of  $V_{0.018}Sb_{1.98}Te_3$ . (a) XAS spectra at V  $L_{23}$  edge and Sb  $M_{45}$  edge. (b) XAS spectra at Te  $M_{45}$  edge. (c) XMCD spectra at V  $L_{23}$  edge and Sb  $M_{45}$  edge. (d) XMCD spectra at Te  $M_{45}$  edge. The spectra showed in (a)-(d) are taken at 5K, 8T. (e) Element-resolved magnetization curves as a function of magnetic field (M-H) at the V-, Sb- and Te-sites taken at 5K.

### 6.3 Experimental results and discussion

Figure 27 shows the element specific magnetic moment of  $V_{0.018}Sb_{1.98}Te_3$ . Clear XAS spectra at V  $L_{23}$  edge, Sb  $M_{45}$  edge and Te  $M_{45}$  edge can be found in Figure 27 (a) and Figure 27(b). The red solid line and blue solid line shows the signal for left- and right-circular polarizations, respectively. Corresponding XMCD spectra are shown in Figure 27 (c) and Figure 27(d). Here we can find that not only V  $L_3$  edge, but also Sb  $M_5$  edge and Te  $M_5$  edge shows XMCD signal. To confirm this result, we took the element-resolved M-H curves, as shown in Figure 27 (e). Although the S/N of Sb and Te are much worse than V (due to the small signal), ferromagnetic hysteresis behavior of all three elements could be observed. From the similar M-H curves, we can assume that the magnetic moments are induced at Sn and Te sites by the doped V atoms. Additionally, considering that the sign of XMCD signal, Sb  $M_5$  edge is opposite to V  $L_3$  edge and Te



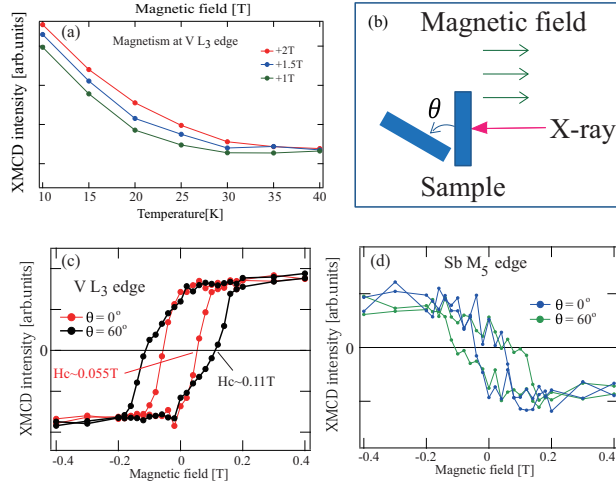


Figure 28: M-T curve and magnetic anisotropy. (a) The XMCD amplitude at the V  $L_3$  edge ( $h\nu=514.5\text{eV}$ ) as a function of temperature (M-T) with 2T, 1.5T and 1T magnetic field. (b) Schematic figure of angle-dependent XMCD measurement. (c) and (d) Angle-dependent M-H curves measured at V- and Sb- sites, respectively.

$M_5$  edge. Here we should notice that V  $L_3$  edge corresponds to the  $p \rightarrow d$  transition while the Sb  $M_5$  edge and Te  $M_5$  edge correspond to the  $d \rightarrow p$  transition. Therefore the Sb 5p and the Te 5p spin is coupled parallel and antiparallel to the V 3d spin, respectively.

For ferromagnetic materials, Curie temperature is an important parameter for application. As shown in Figure 28 (a), M-T curves at V  $L_3$  edge were measured at different magnetic field, including +2T, +1.5T and +1T. Furthermore, to study the magnetic anisotropy, we tilted the sample with  $45^\circ$  and took the XMCD measurement, as shown in Figure 28 (b). Although signal at Te  $M_5$  edge is too weak, we found interesting result at V  $L_3$  edge and Sb  $M_5$  edge. As the coercive force decrease significantly after tilted, the easy axis should be out of plane. If we compare the value of coercive force at V  $L_3$  edge before and after tiled, we can find that it decrease to  $\sim 50\%$ . That means the in-plane magnetism is almost zero, which shows an advantage in realizing QAHE.

## 6.4 Conclusion

V-doped  $\text{Sb}_2\text{Te}_3$  shows ferromagnetism, not only for V, but also for Sb and Te. The same hysteresis behavior of three elements shows that the ferromagnetism of Sb and Te are induced by doped V. Therefore we speculate that the interaction between the Sb(Te) p and V d states is crucial for the long-range magnetic order. Additionally, magnetic

anisotropy shows the easy axis is out-of plane, which is good for realizing QAH effect.

## 7 Summary

To summarize, by combining a series of electron spectroscopy methods, we have studied the electronic and magnetic properties of FMSA  $\text{Ni}_{50}\text{Mn}_{50-x}\text{In}_x$ , topological insulator  $\text{Sb}_2\text{Te}_3$  and  $\text{V}_{0.018}\text{Sb}_{1.98}\text{Te}_3$ .

For  $\text{Ni}_{50}\text{Mn}_{50-x}\text{In}_x$ , we combined hard-X-ray photoelectron spectroscopy and first-principles density-functional calculations. We observed the a temperature induced pseudo gap following the martensite phase transition and found it strongly related to the minority-spin Ni 3d  $e_g$  state located just below  $E_F$ . This pseudogap formation is the origin of higher resistivity and hence the prominent magnetoresistance. The first-principles calculation has shown that the anti-ferromagnetic  $\text{Mn}_{\text{Mn}}\text{-Mn}_{\text{In}}$  spin coupling is preferred in the martensitic phase for  $\text{Ni}_2\text{Mn}_{1.5}\text{In}_{0.5}$ . Such a spin-coupling manner originates from the minority-spin Ni 3d  $e_g$  state as a key ingredient of structural instability. This help us to understand the origin of MPT in  $\text{Ni}_{50}\text{Mn}_{50-x}\text{In}_x$  system and will help for the realization of magnetic refrigeration.

For topological insulator  $\text{Sb}_2\text{Te}_3$ , we employed the trARPES studying the unoccupied state as well as the electron dynamics near Dirac node. A population inversion which leads to an amazing hourglass effect was observed at Dirac node. Combing with our simulation, we concludes that the low density of state near Dirac node is responsible for the population inversion. This is important for understanding the electron dynamics of topological insulator, especially when Dirac node is above Fermi energy.

For magnetic doped topological insulator  $\text{V}_{0.018}\text{Sb}_{1.98}\text{Te}_3$ , with XMCD, we studied the elemental specified magnetic property. V, Sb and Te atoms showed clear hysteresis behavior which originates from ferromagnetism. The ferromagnetism of Sb and Te induced by doped V atoms illustrate that not only the magnetic moments for the V dopant d states but also the Sb and Te p states in the host lattice contribute to the ferromagnetism. By tilting the sample, we find the easy axis is out of plane. This result is consistent with the QAHE in V-doped  $(\text{BiSb})_2\text{Te}_3$  and expand our knowledge of QAHE.

## Acknowledgement

At first, I would like to give special appreciation to my supervisor Prof. Akio Kimura and Prof. Masaki Taniguchi who allowed an opportunity of studying in such a great environment that I concentrate to progress this project. I would like to express my grateful for the kind, patient and intellectual guidance from Prof. Kimura. His positive attitude encouraged me every time when I feel depressed. I would like to express my gratitude to the senior students, Dr. Kenta Kuroda for his kind advice for sample growth and spectroscopy studies, Dr. Mao Ye for his great help in STM, XMCD, ARPES studies and daily life. I would like to appreciate Dr. Yukiaki Ishida for his great support for the trARPES experiment and discussion. It is my pleasure to acknowledge the support from Dr. Yukiharu Takeda, Dr. Yuji Saitoh and Dr. Shigenori Ueda in SPring-8. The work will be impossible without the support of high quality samples, as well as fruitful discussion from Dr. Oleg Tereshchenko, Prof. Shan Qiao, Prof. Yoshio Miura, Prof. Masafumi Shirai, Prof. Rie Yamauchi Umetsu, Prof. Ryosuke Kainuma and Prof. Takeshi Kanomata.

I could send a great time in graduate school of science in Hiroshima University under kind support from Prof. Taichi Okuda, Prof. Ino, Dr. Koji Miyamoto, Dr. Munisa Nurmatamat and all members in the group. I would like to thank to Dr. Jiang, Dr. Utsumi, Mr. Miyahara, Mr. Okamoto, Mr. Warashina, Mr. Shirai, Mr. Sumida, Mr. Chen, Mr. Kubo, Mr. Yori, Mr. Umut for their great advices and cooperation from physics to daily life. I also would like to thank to the Japanese Government(MONBUKAGAKUSHO:MEXT) Scholarship for the financial support

Finally, I would like to thank for my parents. Their material and spiritual support from China accompany with me during the whole five years. Without that all the work can not be accomplished.

20, June, 2015

Siyuan Zhu

## References

- [1] K. A. Gschneidner Jr, V. K. Pecharsky and A. O. Tsokol Recent developments in magnetocaloric materials. *Rep. Prog. Phys.* **68**, 1479 (2005)
- [2] W. F. Giauque A thermodynamic treatment of certain magnetic effects. A proposed method of producing temperatures considerably below  $1^\circ$  absolute. *J. Am. Chem. Soc.* **49**, 1864 (1927)
- [3] O. Gutfleisch et al. Magnetic materials and devices for the 21st century: stronger, lighter, and more energy efficient. *Adv. Mater.* **23**, 821 (2011)
- [4] V. Basso, C. P. Sasso and M. LoBue Thermodynamic aspects of first-order phase transformations with hysteresis in magnetic materials. *J. Magn. Magn. Mater.* **316**, 262(2007)
- [5] L. Caron et al. On the determination of the magnetic entropy change in materials with first-order transitions. *J. Magn. Magn. Mater.* **321**, 3559 (2009)
- [6] M. V. Yablonskikh et al. X-ray  $2p$  photoelectron and  $L_\alpha$  resonant x-ray emission spectra of the  $3d$  metals in  $\text{Ni}_2\text{MnZ}$  ( $Z = \text{In, Sn, Sb}$ ) Heusler alloys. *Phys. Rev. B* **74**, 085103 (2006)
- [7] R. Kainuma et al. Magnetic-field-induced shape recovery by reverse phase transformation. *Nature* **439**, 957 (2006)
- [8] J. Liu, T. Gottschall, K. P. Skokov, J. D. Moore and O. Gutfleisch Giant magnetocaloric effect driven by structural transitions. *Nature Materials* **11**, 620 (2012)
- [9] S. R. Barman, S. Banik and A. Chakrabarti Structural and electronic properties of  $\text{Ni}_2\text{MnGa}$ . *Phys. Rev. B* **72**, 184410 (2005)
- [10] A. Ayuela, J. Enkovaara, K. Ullakko and R. M. Nieminen Structural properties of magnetic Heusler alloys. *J. Phys. Condens. Matter* **11**, 2017 (1999)

- [11] A. Ayuela, J. Enkovaara and R. M. Nieminen *Abinitio* study of tetragonal variants in Ni<sub>2</sub>MnGa alloy. *J. Phys. Condens. Matter* **14**, 5325 (2002)
- [12] A. Planes, L. Mañosa and M. Acet Magnetocaloric effect and its relation to shape-memory properties in ferromagnetic Heusler alloys. *J. Phys. Condens. Matter* **21**, 233201 (2009)
- [13] C.-L. Tan, Y.-W. Huang, X.-H. Tian, J.-X. Jiang and W. Cai Origin of magnetic properties and martensitic transformation of Ni-Mn-In magnetic shape memory alloys. *Appl. Phys. Lett.* **100**, 132402 (2012)
- [14] C.-X. Liu, X.-L. Qi, X. Dai, Z. Fang and S.-C. Zhang Quantum anomalous Hall effect in Hg<sub>1-y</sub>Mn<sub>y</sub>Te quantum wells. *Phys. Rev. Lett.* **101**, 146802 (2008).
- [15] C.-Z. Chang et al. Experimental observation of the quantum anomalous Hall effect in a magnetic topological insulator. *Science* **12**, 167 (2013)
- [16] M. A. Paalanen, D. C. Tsui and A. C. Gossard Quantized Hall effect at low temperatures. *Phys. Rev. B* **25**, 5566 (1982)
- [17] H.L. Stormer, D.C. Tsui and A.C. Gossard The fractional quantum Hall effect. *Rev. Mod. Phys.* **71**, 298 (1999)
- [18] P. J. Webster, K. R. A. Ziebeck, S. L. Town and M. S. Peak Magnetic order and phase transformation in Ni<sub>2</sub>MnGa. *Philos. Mag. B* **49**, 295 (1984)
- [19] K. Ullakko, J.-K. Huang, C. Kantner, R. C. O’Handley and V. V. Kokorin Large magnetic-field-induced strains in Ni<sub>2</sub>MnGa single crystals. *Appl. Phys. Lett.* **69**, 1966 (1996)
- [20] A. Sozinov, A. A. Likchachev, N. Lanska and K. Ullakko Giant magnetic-field-induced strain in NiMnGa seven-layered martensitic phase. *Appl. Phys. Lett.* **80**, 1746 (2002)
- [21] A. Sozinov, N. Lanska, A. Soroka and W. Zou 12% magnetic field-induced strain in Ni-Mn-Ga-based non-modulated martensite. *Appl. Phys. Lett.* **102**, 021902 (2013)

- [22] Y. Sutou et al. Magnetic and martensitic transformations of NiMnX (X= In, Sn, Sb) ferromagnetic shape memory alloys. *Appl. Phys. Lett.* **85**, 4358 (2004)
- [23] T. Krenke et al. Inverse magnetocaloric effect in ferromagnetic Ni-Mn-Sn alloys. *Nature Mater.* **4** 450 (2005)
- [24] S.-Y. Yu et al. Large magnetoresistance in single-crystalline Ni<sub>50</sub>Mn<sub>50-x</sub>In<sub>x</sub> alloys (x= 14–16) upon martensitic transformation. *Appl. Phys. Lett.* **89** 162503 (2006)
- [25] B. Zhang, X.-X. Zhang, S.-Y. Yu, J.-L. Chen, Z.-X. Cao and G.-H Wu Giant magnetothermal conductivity in the NiCMnCIn ferromagnetic shape memory alloys. *Appl. Phys. Lett.* **91** 012510 (2007)
- [26] H. E. Karaca, I. Karaman, B. Basaran, Y. Ren, Y. I. Chumlyakov and H. J. Maier Magnetic field-induced phase transformation in NiMnCoIn magnetic shape-memory alloys a new actuation mechanism with large work output. *Adv. Funct. Mater.* **19**, 983 (2009)
- [27] M. Ye et al. Role of electronic structure in the Martensitic phase transition of Ni<sub>2</sub>Mn<sub>1+x</sub>Sn<sub>1-x</sub> studied by hard-X-ray photoelectron spectroscopy and *ab initio* calculation. *Phys. Rev. Lett.* **104**, 176401 (2010)
- [28] K. Oikawa et al. Effect of magnetic field on martensitic transition of Ni<sub>46</sub>Mn<sub>41</sub>In<sub>13</sub> Heusler alloy. *Appl. Phys. Lett.* **88**, 122507 (2006)
- [29] T. Kanomata et al. Magnetic properties on shape memory alloys Ni<sub>2</sub>Mn<sub>1+x</sub>In<sub>1-x</sub>. *J. Mag. Mag. Mater.* **321**, 773 (2009)
- [30] W. Ito, X. Xu, R. Y. Umetsu, T. Kanomata, K. Ishida and R. Kainuma Concentration dependence of magnetic moment in Ni<sub>50-x</sub>Co<sub>x</sub>Mn<sub>50-y</sub>Z<sub>y</sub> (Z=In,Sn) Heusler alloys. *Appl. Phys. Lett.* **97**, 242512 (2010)
- [31] S. Ueda et al. Present Status of the NIMS Contract Beamline BL15XU at SPring-8. *AIP Conf. Proc.* **1234**, 403 (2010)

- [32] S. Ueda Application of hard x-ray photoelectron spectroscopy to electronic structure measurements for various functional materials. *J. Electron. Spectrosc. Relat. Phenom.* **190**, 235 (2013)
- [33] G. Kresse and J. Hafner Efficient iterative schemes for *abinitio* total-energy calculations using a plane-wave basis set. *Phys. Rev. B* **47**, 558 (1993)
- [34] G. Kresse and J. Furthmüller Efficiency of *ab – initio* total energy calculations for metals and semiconductors using a plane-wave basis set. *Comput. Mater. Sci.* **6**, 15 (1996)
- [35] J. P. Perdew, K. Burke and M. Ernzerhof Generalized gradient approximation made simple. *Phys. Rev. Lett.* **77**, 3865 (1996)
- [36] P. E. Blöchl, Projector augmented-wave method. *Phys. Rev. B* **50**, 17953 (1994)
- [37] G. Kresse and D. Joubert From ultrasoft pseudopotentials to the projector augmented-wave method. *Phys. Rev. B* **59**, 1758 (1999)
- [38] C. P. Opeil et al. Combined experimental and theoretical investigation of the premartensitic transition in Ni<sub>2</sub>MnGa *Phys. Rev. Lett.* **100**, 165703 (2008)
- [39] V. D. Buchelnikov, V. V. Sokolovskiy, M. A. Zagrebin, M. A. Tufatullina and P. Entel First principles investigation of structural and magnetic properties of Ni-Co-Mn-In Heusler alloys. *J. Phys. D: Appl. Phys.* **48**, 164005 (2015)
- [40] L. Fu, C. Kane and E. Mele Topological insulators in three dimensions. *Phys. Rev. Lett.* **98**, 106803 (2007).
- [41] H. Zhang *et al.* Topological insulators in Bi<sub>2</sub>Se<sub>3</sub>, Bi<sub>2</sub>Te<sub>3</sub> and Sb<sub>2</sub>Te<sub>3</sub> with a single Dirac cone on the surface. *Nature Phys.* **5**, 438–442 (2009).
- [42] Y. L. Chen *et al.* Experimental realization of a three-dimensional topological insulator Bi<sub>2</sub>Te<sub>3</sub>. *Science* **325**, 178–181 (2009).
- [43] Y. Xia *et al.* Observation of a large-gap topological-insulator class with a single Dirac cone on the surface. *Nature Phys.* **5**, 398–402 (2009).



- [44] X. L. Qi and S. C. Zhang Topological insulators and superconductors. *Rev. Mod. Phys.* **83**, 1057 (2011).
- [45] D. Hsieh *et al.* A tunable topological insulator in the spin helical Dirac transport regime. *Nature* **460**, 1101–1105 (2009).
- [46] D. Hsieh *et al.* Observation of unconventional quantum spin textures in topological insulators. *Science* **323**, 919–922 (2009).
- [47] P. Roushan *et al.* Topological surface states protected from backscattering by chiral spin texture. *Nature* **460**, 1106 (2009).
- [48] Y. Xia *et al.* Observation of a large-gap topological-insulator class with a single Dirac cone on the surface. *Nature Phys.* **5**, 398–402 (2009).
- [49] D. Hsieh *et al.* Observation of time-reversal-protected single-Dirac-cone topological insulator states in  $\text{Bi}_2\text{Te}_3$  and  $\text{Sb}_2\text{Te}_3$ . *Phys. Rev. Lett.* **5**, 146401 (2009).
- [50] T. Sato *et al.* Direct evidence for the Dirac-cone topological surface states in the ternary chalcogenide  $\text{TlBiSe}_2$ . *Phys. Rev. Lett.* **105**, 136802 (2010).
- [51] K. Kuroda *et al.* Experimental verification of  $\text{PbBi}_2\text{Te}_4$  as a 3D topological insulator. *Phys. Rev. Lett.* **108**, 206803 (2012).
- [52] D. Niesner *et al.* Bulk and surface electron dynamics in a p-type topological insulator  $\text{SnSb}_2\text{Te}_4$ . *Phys. Rev. B* **89**, 081404 (2014).
- [53] S. A. Wolf *et al.* Spintronics: a spin-based electronics vision for the future. *Science* **294**, 1488 (2001).
- [54] D. Kong *et al.* Ambipolar field effect in the ternary topological insulator  $(\text{Bi}_x\text{Sb}_{1-x})_2\text{Te}_3$  by composition tuning. *Nature Nanotech.* **6**, 705 (2011).
- [55] F. Xiu *et al.* Manipulating surface states in topological insulator nanoribbons. *Nature Nanotech.* **6**, 216 (2011).

- [56] J. W. McIver, D. Hsieh, H. Steinberg, P. Jarillo-Herrero and N. Gedik Control over topological insulator photocurrents with light polarization. *Nature Nanotech* **7**, 96.
- [57] S. Kim *et al.* Robust protection from backscattering in the topological insulator  $\text{Bi}_{1.5}\text{Sb}_{0.5}\text{Te}_{1.7}\text{Se}_{1.3}$ . *Phys. Rev. Lett.* **112**, 136802 (2014).
- [58] J. C. Johannsen *et al.* Direct view of hot carrier dynamics in graphene. *Phys. Rev. Lett.* **111**, 027403 (2013).
- [59] J. A. Sobota *et al.* Ultrafast electron dynamics in the topological insulator  $\text{Bi}_2\text{Se}_3$  studied by time-resolved photoemission spectroscopy. *J. Electron. Spectrosc. Relat. Phenom.* **195**, 249–257 (2014).
- [60] J. A. Sobota *et al.* Ultrafast optical excitation of a persistent surface-state population in the topological insulator  $\text{Bi}_2\text{Se}_3$ . *Phys. Rev. Lett.* **108**, 117403 (2012).
- [61] Y. H. Wang *et al.* Measurement of intrinsic Dirac fermion cooling on the surface of the topological insulator  $\text{Bi}_2\text{Se}_3$  using time-resolved and angle-resolved photoemission spectroscopy. *Phys. Rev. Lett.* **109**, 127401 (2012).
- [62] A. Crepaldi *et al.* Ultrafast photodoping and effective Fermi-Dirac distribution of the Dirac particles in  $\text{Bi}_2\text{Se}_3$ . *Phys. Rev. B* **86**, 205133 (2012).
- [63] Y.-H. Wang, H. Steinberg, P. Jarillo-Herrero and N. Gedik Observation of Floquet-Bloch States on the Surface of a Topological Insulator. *Science* **342**, 453 (2013).
- [64] J. A. Sobota *et al.* Distinguishing bulk and surface electron-phonon coupling in the topological insulator  $\text{Bi}_2\text{Se}_3$  using time-resolved photoemission spectroscopy. *Phys. Rev. Lett.* **113**, 157401 (2014).
- [65] M. Hajlaoui *et al.* Tuning a Schottky barrier in a photoexcited topological insulator with transient Dirac cone electron-hole asymmetry. *Nat. Commun.* **5**, 3003 (2014).
- [66] A. Kirilyuk, A. V. Kimel and T. Rasing Ultrafast optical manipulation of magnetic order. *Rev. Mod. Phys.* **82**, 2731 (2010).

- [67] D. Hsieh *et al.* Selective probing of photoinduced charge and spin dynamics in the bulk and surface of a topological insulator. *Phys. Rev. Lett.* **107**, 077401 (2011).
- [68] C.-W. Luo *et al.* Snapshots of Dirac fermions near the Dirac point in topological insulators. *Nano Lett.* **13**, 5797 (2013).
- [69] Y. Ishida *et al.* Time-resolved photoemission apparatus achieving sub-20-meV energy resolution and high stability. *Rev. Sci. Instrum.* **85**, 123904 (2014).
- [70] J. A. Sobota *et al.* Direct optical coupling to an unoccupied Dirac surface state in the topological insulator Bi<sub>2</sub>Se<sub>3</sub>. *Phys. Rev. Lett.* **111**, 136802 (2013).
- [71] L. Cheng *et al.* High Curie temperature Bi<sub>1.85</sub>Mn<sub>0.15</sub>Te<sub>3</sub> nanoplates. *J. Am. Chem. Soc.* **134**, 18920 (2012)
- [72] P. Cheng *et al.* Landau quantization of topological surface states in Bi<sub>2</sub>Se<sub>3</sub>. *Phys. Rev. Lett.* **105**, 076801 (2010).
- [73] T. Hanaguri, K. Igarashi, M. Kawamura, H. Takagi and T. Sasagawa Momentum-resolved Landau-level spectroscopy of Dirac surface state in Bi<sub>2</sub>Se<sub>3</sub>. *Phys. Rev. B* **82**, 081305 (2010).
- [74] Y. Jiang *et al.* Landau quantization and the thickness limit of topological insulator thin films of Sb<sub>2</sub>Te<sub>3</sub>. *Phys. Rev. Lett.* **108**, 016401 (2012).
- [75] Y. Jiang *et al.* Fermi-Level tuning of epitaxial Sb<sub>2</sub>Te<sub>3</sub> thin films on graphene by regulating intrinsic defects and substrate transfer doping. *Phys. Rev. Lett.* **108**, 066809 (2012).
- [76] J. Reimann, J. Gudde, K. Kuroda, E. V. Chulkov and U. Hofer Spectroscopy and dynamics of unoccupied electronic states of the topological insulators Sb<sub>2</sub>Te<sub>3</sub> and Sb<sub>2</sub>Te<sub>2</sub>S. *Phys. Rev. B* **90**, 081106 (2014).
- [77] S. M. Sze, *Physics of Semiconductor Devices* (Wiley, New York, 1981).
- [78] M. Levinshtein, J. Kostamovaara and S. Vainshtein, *Breakdown Phenomena in Semiconductors and Semiconductor Devices* (World Scientific, London, 2005).

- [79] Y. V. Nazarov and J. Danon *Advanced Quantum Mechanics: A Practical Guide* (Cambridge University Press, Cambridge, 2013).
- [80] W. S. Fann, R. Storz, H. W. K. Tom and J. Bokor, Electron thermalization in gold. *Phys. Rev. B* **46**, 13592–13595 (1992).
- [81] T. Li *et al.* Femtosecond population inversion and simulated emission of dense Dirac fermions in graphene. *Phys. Rev. Lett.* **108**, 167401 (2012).
- [82] H.-J. Zhang, C.-X. Liu, X.-L. Qi, X. Dai, Z. Fang and S.-C. Zhang Topological insulators in  $\text{Bi}_2\text{Se}_3$ ,  $\text{Bi}_2\text{Te}_3$  and  $\text{Sb}_2\text{Te}_3$  with a single Dirac cone on the surface. *Nat. Phys.* **5**, 438 (2009).
- [83] T. Valla, Z.-H. Pan, D. Gardner, Y. S. Lee and S. Chu, Photoemission spectroscopy of magnetic and nonmagnetic impurities on the surface of the  $\text{Bi}_2\text{Se}_3$  topological insulator. *Phys. Rev. Lett.* **108**, 117601 (2012).
- [84] K. Ito *et al.* X-ray magnetic circular dichroism of ferromagnetic  $\text{Co}_4\text{N}$  epitaxial films on  $\text{SrTiO}_3(001)$  substrates grown by molecular beam epitaxy. *Appl. Phys. Lett.* **99**, 252501 (2011).


# Part II

## 公表論文

- (1) Ultrafast electron dynamics at the Dirac node of the topological insulator  $\text{Sb}_2\text{Te}_3$   
**S.-Y. Zhu**, Y. Ishida, K. Kuroda, K. Sumida, M. Ye, J. Wang, H. Pan, M. Taniguchi, S. Qiao, S. Shin & A. Kimura  
*Scientific Reports* **5**, 13213 (2015)
- (2) Drastic change in density of states upon martensitic phase Transition for Metamagnetic Shape Memory Alloy  $\text{Ni}_2\text{Mn}_{1+x}\text{In}_{1-x}$   
**S.-Y. Zhu**, M. Ye, K. Shirai, M. Taniguchi, S. Ueda, Y. Miura, M. Shirai, R. Y. Umetsu, R. Kainuma, T. Kanomata and A. Kimura  
*Journal of Physics: Condensed Matter* **27**, 362201 (2015)



# SCIENTIFIC REPORTS



OPEN

## Ultrafast electron dynamics at the Dirac node of the topological insulator $\text{Sb}_2\text{Te}_3$

Received: 20 March 2015

Accepted: 10 July 2015

Published: 21 August 2015

Siyuan Zhu<sup>1</sup>, Yukiaki Ishida<sup>2</sup>, Kenta Kuroda<sup>1</sup>, Kazuki Sumida<sup>1</sup>, Mao Ye<sup>3</sup>, Jiajia Wang<sup>4</sup>, Hong Pan<sup>5</sup>, Masaki Taniguchi<sup>2</sup>, Shan Qiao<sup>3,4</sup>, Shik Shin<sup>2</sup> & Akio Kimura<sup>1</sup>

Topological insulators (TIs) are a new quantum state of matter. Their surfaces and interfaces act as a topological boundary to generate massless Dirac fermions with spin-helical textures. Investigation of fermion dynamics near the Dirac point (DP) is crucial for the future development of spintronic devices incorporating topological insulators. However, research so far has been unsatisfactory because of a substantial overlap with the bulk valence band and a lack of a completely unoccupied DP. Here, we explore the surface Dirac fermion dynamics in the TI  $\text{Sb}_2\text{Te}_3$  by time- and angle-resolved photoemission spectroscopy (TrARPES).  $\text{Sb}_2\text{Te}_3$  has an in-gap DP located completely above the Fermi energy ( $E_F$ ). The excited electrons in the upper Dirac cone stay longer than those below the DP to form an inverted population. This was attributed to a reduced density of states (DOS) near the DP.

Three-dimensional TIs have emerged as a new state of condensed matter and are characterized by non-trivial gapless surface states (SS) that occur because of a strong spin-orbit coupling. The SS traversing the band gap between the bulk valence band (VB) and conduction band (CB) can be described by the Dirac equation for massless fermions<sup>1–5</sup>. Additionally, the SS are spin-polarized and the spin orientations are fixed with respect to their momenta<sup>6–8</sup>. Such a peculiar electronic structure, which originates from its  $\pi$  Berry phase, results in an anti-localization of surface electrons with a suppressed backscattering probability. A number of 3D TIs, including  $\text{Bi}_2\text{Se}_3$ ,  $\text{Bi}_2\text{Te}_3$ ,  $\text{Sb}_2\text{Te}_3$ ,  $\text{TlBiSe}_2$ ,  $\text{PbBi}_2\text{Te}_4$  and  $\text{SnSb}_2\text{Te}_4$ , have been discovered experimentally<sup>9–13</sup>. TIs have recently attracted much attention because of their possible applications in spintronic devices and in ultra-fast and fault tolerant quantum computation<sup>14–17</sup>. When aiming to improve such novel device applications incorporating TIs, it is important to understand the hot carrier dynamics of the surface Dirac fermions.

Angle resolved photoemission spectroscopy (ARPES) implemented by a pump-and-probe method is a powerful tool to study the unoccupied states and electron dynamics with energy and momentum resolutions. Many groups have made great progress of TrARPES on TIs<sup>18–28</sup>. Recently, TrARPES measurements at the sub-20-meV energy resolutions became possible<sup>29,30</sup>. This enabled us to observe the electron dynamics near the DP in detail. To examine the flow of electrons across the DP, we need an initial state situation (for example, before pumping) in which both the upper and lower parts of the Dirac cone are empty. This could be realized in *p*-type TIs, wherein the DP is located above  $E_F$ . Graphene, whose DP is almost at or below  $E_F$ , is therefore not suitable for this purpose. The *p*-type  $\text{Bi}_2\text{Se}_3$  is also unsuitable because the lower part of Dirac cone is not energetically isolated from the bulk valence band<sup>31</sup>. This

<sup>1</sup>Graduate School of Science, Hiroshima University, 1-3-1 Kagamiyama, Higashi-Hiroshima, Hiroshima 739-8526, Japan. <sup>2</sup>Institute for Solid State Physics, the University of Tokyo, 5-1-5, Kashiwa-no-ha, Chiba 277-8581, Japan.

<sup>3</sup>State Key Laboratory of Functional Materials for Informatics, Shanghai Institute of Microsystem and Information Technology, Chinese Academy of Sciences, 865 Chang Ning Road, Shanghai 200050, China. <sup>4</sup>School of physical science and technology, Shanghai Tech University, 319 Yueyang Road, Shanghai 200031, China. <sup>5</sup>Department of Physics, State Key Laboratory of Surface Physics, and Laboratory of Advanced Materials, Fudan University, Shanghai 200433, China. Correspondence and requests for materials should be addressed to S.Z. (email: zhusiyuan@hiroshima-u.ac.jp)

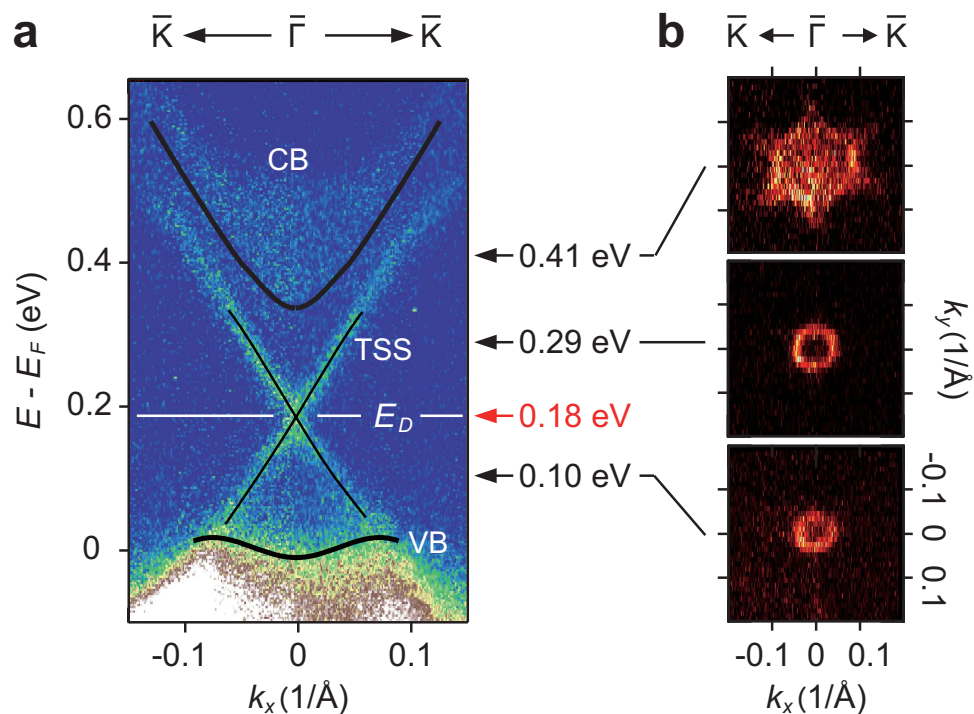


**Figure 1.** Band structure of  $\text{Sb}_2\text{Te}_3$  revealed into the unoccupied side. (a) The TrARPES images of  $\text{Sb}_2\text{Te}_3$  recorded at  $t = 0.4$  ps along the  $\bar{\Gamma} - \bar{K}$  direction. (b) Constant energy maps at 100, 290 and 410 meV.

feature can also be seen from the absence of the Landau level quantization in the lower part of the surface Dirac cone, while it is visible above the DP<sup>32,33</sup>.

In contrast,  $\text{Sb}_2\text{Te}_3$  shows surface Landau quantizations over the energy range of  $\sim 240$  meV (120 meV below and 120 meV above the DP)<sup>34,35</sup>. Here, the Dirac cone SS is separated from the bulk states, which enables us to study an isolated Dirac cone. Secondly, a  $\text{Sb}_2\text{Te}_3$  single crystal is naturally *p*-doped, and the DP is located above the  $E_F$ . Therefore, we do not need to dope any element into the mother crystal. This is advantageous when attempting to increase the quality of the sample. Having considered the above-mentioned characteristics,  $\text{Sb}_2\text{Te}_3$  is suitable for the present study.

In this study, we investigated the unoccupied bulk and surface states of  $\text{Sb}_2\text{Te}_3$  using TrARPES. The electron dynamics below and above the DP were also revealed. One of the most striking findings is that the decay of the pump-induced carriers are bottlenecked at the DP, so that the hot carriers in the upper part of the SS stay longer than those in the lower part.

## Results and Discussion

By pumping the electrons into the unoccupied side, we observed a linear Dirac cone SS as shown in Fig. 1(a). Here, the pump-and-probe delay,  $t$ , was set to 0.4 ps. The DP is located  $\sim 180$  meV above the  $E_F$  and the Dirac velocity was estimated to be  $\sim 2.3 \times 10^5$  m/s. We found that both the upper and lower parts of the Dirac cone (UDC and LDC, respectively) were clearly visible above  $E_F$  and they do not overlap with the bulk continuum states. Figure 1(b) shows the constant energy contours at 100, 290 and 410 meV with respect to the Fermi energy. With increasing the energy, the SS evolves from a circular to hexagonal shape. The isotropic constant surface can be observed both below and above the DP within the bulk energy gap. The hexagonal warping of the constant energy surfaces is quite small as long as bulk continuum states do not overlap with the SS. In the previous STM study on  $\text{Sb}_2\text{Te}_3$ , the DP is 80 meV higher, whereas the energy range of the SS ( $\sim 120$  meV above and below the DP) is consistent with the present observations<sup>34,35</sup>; see Fig. 1(a). With such an ideal situation, there is a good opportunity to study the carrier dynamics of UDC and LDC separately, where interference from the bulk states is minimized.

To study the pump-induced dynamics of the surface Dirac fermions, we altered the pump and probe delay and investigated the time dependent variations in the TrARPES images. Figure 2(a) shows the difference image along the  $\bar{\Gamma} - \bar{K}$  line measured at  $t = 0.4$  ps. Both the Dirac cone SS and unoccupied bulk state were clearly observed. To show the energy dependent dynamics, we set energy and momentum frames [A to I: see Fig. 2(a)] and plotted the intensity variation in each frame as functions of  $t$  [see Fig. 2(b)]. Also, to show the variation in the different bands more clearly, we show the original and difference images for typical delay times in Fig. 2(c) and in a Supplementary Movie S1. Here we note that



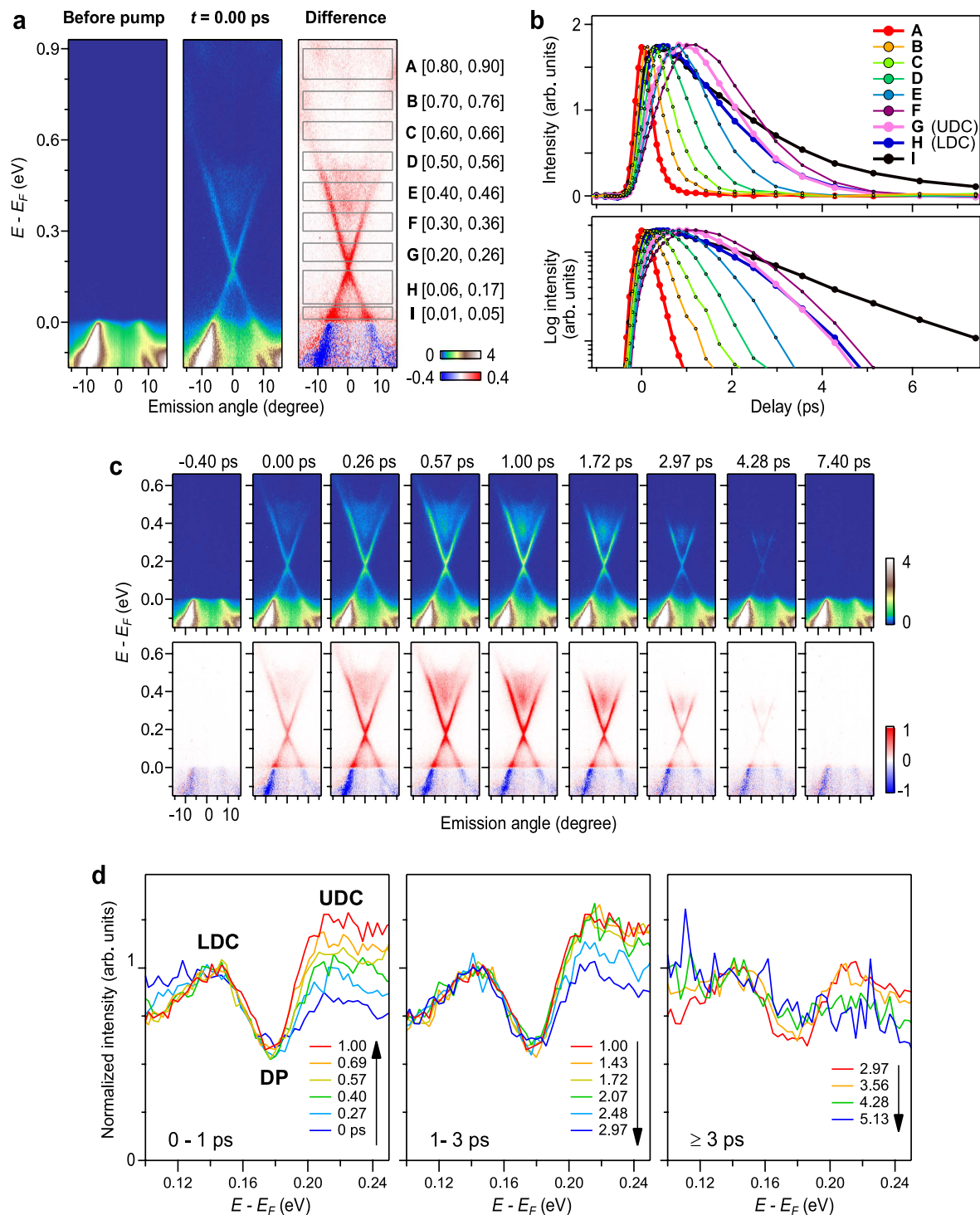


**Figure 2. TrARPES of  $\text{Sb}_2\text{Te}_3$ .** (a) TrARPES images recorded along the  $\bar{\Gamma} - \bar{K}$  line recorded before pump (left; images recorded at  $\leq 0.6$  ps were averaged), at 0 ps (middle), and their difference (right panel). The frames A to I span in the angular range of  $\pm 15$  degrees and in the energy ranges of [0.80, 0.90], [0.70, 0.76], [0.60, 0.66], [0.50, 0.56], [0.40, 0.46], [0.30, 0.36], [0.20, 0.26], [0.06, 0.17] and [0.01, 0.05] (in units of eV), respectively. (b) Intensity variation line profiles. Integrated intensity in each of the frames A to I is plotted as functions of delay time in a linear (upper panel) and in a logarithmic scale (lower panel). (c) TrARPES images. Upper and lower panels show TrARPES and difference to that recorded before pump. Full set of TrARPES and difference images are provided as a Supplementary Movie S1. (d) EDCs (integration of TrARPES images over  $\pm 15$  degrees) recorded at  $0 \leq t \leq 1.00$  ps (left),  $1.00 \leq t \leq 2.97$  ps (middle), and at  $2.97 \leq t \leq 5.13$  ps (right panel). Here, the EDCs are normalized to the area around the peak in the LDC region. For the full set of EDCs, see Supplementary Movie S2.

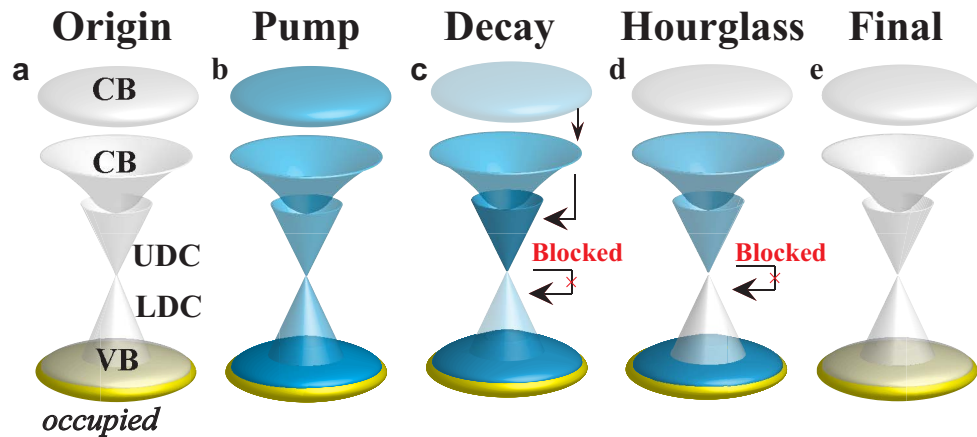


**Figure 3. Schematics of the pump and decay processes.** The state before pumping (a), upon the pump (b), subsequent decay (c) leading to an hourglass-shaped electron distribution (d), and the final state (e). The colour gradation represents the electron density.

the intensity variation line profiles of bulk and surface states at the same energy overlapped each other as shown in the Supplementary Fig. S1.

In the highest energy region A, we observed a fast rise of intensity that was limited by the time resolution without significant delay. The intensity variation was almost symmetric about  $t = 0$ . This indicates that the intensity variation in region A comprises two processes. One is the instantaneous filling of the states by direct excitations and the other one is the very fast flow of the excited electrons out of region A into the lower energy states. Because the flow of electrons into region A from higher energies is negligibly small, the line shape does not show significant asymmetric tailing into  $t > 0$ .

Next, we compared the energy regions A, B, C, D, E and F, which are overlapped to the conduction band. The duration of the intensity variation became longer as the DP was approached. This indicates that there was an energy dependence on the transfer rate of electrons: The net flow rate of electrons from high to low energy decreased when the Dirac point was approached. This can occur because the available phase space diminishes on the approach of the DP, and so the hot carriers pile up around the bottom of the UDC. Similar behaviour was observed above the DP for  $\text{Bi}_2\text{Se}_3$ <sup>19</sup>. Considering that the behaviour can be represented by an exponential decay, the decay constant,  $\tau$ , of the different regions varied from 0.2 to 2 ps, which is comparable to a recent study on  $\text{Sb}_2\text{Te}_3$ <sup>36</sup>.

The most striking observation was found across the DP, namely in the intensity variations of regions G and H. Although region H in the LDC was located lower in energy than G in the UDC, the intensity after  $\sim 1$  ps diminished faster in H than in G as shown in Fig. 2(b). Figure 2(d) shows EDCs (integral of the TrARPES images over  $\pm 15$  degrees) normalized to the peak in the LDC region. From  $\sim 0.4$  to  $\sim 3$  ps, the spectral intensity in the UDC region is higher than that in the LDC region. We take this as evidence for the population inversion across the DP. Note, if the electron distribution was obeying a thermal Fermi-Dirac function, there would be no crossings between the intensity variation line profiles at different energies, which is opposed to the case seen in Fig. 2(b); also see Supplementary Fig. S2. After  $\sim 3$  ps, the intensity in the UDC region becomes smaller than that in the LDC region [right panel of Fig. 2(d)]. Correspondingly, the intensity variation line profiles of regions G and H shown in Fig. 2(d) almost overlap each other after  $\sim 3$  ps.

The population inversion can occur across the DP because the node acts as a bottleneck for the electrons flowing from high to low energies: The low DOS near the DP is considered to play a key role in the formation of the population inversion. In order to support this view, we solved a rate equation under DOS having some structures. We find that an inverted population can be formed when the DOS has a valley-like structure similar to the case having a DP; see Fig. S3 in the supplementary file. The simulation also shows that, after the ‘electron jam’ near the node is cleared, the decay profiles across the node become similar, which qualitatively explicates the decay-profile behaviour after  $\sim 3$  ps seen in Fig. 2(b).

We also observed that the rise time of the intensity in region I, which is close to  $E_F$  is faster than those in the UDC regions. The fast intensity rise around  $E_F$  is attributed to the impact ionization: The direct photo-excitation accompanies the low energy excitations across  $E_F$ <sup>37–39</sup>. The effect of impact ionization is limited to  $\lesssim 50$  meV and is similar to the Fermi cutoff broadening, as seen in time-resolved photoemission spectra of metals<sup>40</sup>. Because the effect of impact ionization occurs only in the vicinity of  $E_F$ , the carrier dynamics in the SS are less affected by the impact ionization.

Schematics of the pump and decay processes from the state before pumping to the final state are shown in Fig. 3. As shown in Fig. 3(b), the direct photo-excitation from the occupied to the unoccupied states is accompanied by the impact ionization. During the decay [Fig. 3(c)], the flow of electrons from

high to low energy is bottlenecked near the DP to result in the hourglass-shaped electron distribution shown in Fig. 3(d).

## Conclusion

The conclusion is threefold. First, TrARPES on  $\text{Sb}_2\text{Te}_3$  revealed the surface state Dirac cone in the unoccupied region. It was found to be isotropic within the bulk energy gap. Second, a rapid intensity increase was found near  $E_F$ , which was caused by the creation of a large number of low energy electron-hole pairs due to impact ionization. Third, we found the spectral intensity inversion at  $\sim 0.4$  to  $\sim 3$  ps across the DP. The population inversion across the Dirac dispersion may be used as an optical gain medium for broad band lasing if the duration of the inversion can be elongated<sup>41</sup>, for example, by continuously injecting carriers into the UDC.

## Methods

The  $\text{Sb}_2\text{Te}_3$  single crystal was grown by the Bridgeman method. The results of electron probe micro analysis (EPMA) showed an atomic ratio of Sb:Te = 2.03:2.97. The experiment was performed with linearly polarized 5.98 (probe) and 1.5 eV (pump) pulses derived from a Ti:sapphire laser system operating at a repetition rate of 250 kHz<sup>30</sup>. The photoelectron kinetic energy and emission angle were resolved using a hemispherical electron analyser. The measurement was done at 8 K with an energy resolution of  $\sim 15$  meV. The origin of the pump-and-probe delay ( $t = 0$ ) and the time resolution of 250 fs was determined from the TrARPES signal of graphite attached next to the sample. The spot diameters of the pump and probe were 0.5 and 0.3 mm, respectively.

## References

1. Fu, L., Kane, C. & Mele, E. Topological insulators in three dimensions. *Phys. Rev. Lett.* **98**, 106803 (2007).
2. Zhang, H. *et al.* Topological insulators in  $\text{Bi}_2\text{Se}_3$ ,  $\text{Bi}_2\text{Te}_3$  and  $\text{Sb}_2\text{Te}_3$  with a single Dirac cone on the surface. *Nature Phys.* **5**, 438–442 (2009).
3. Chen, Y. L. *et al.* Experimental realization of a three-dimensional topological insulator  $\text{Bi}_2\text{Te}_3$ . *Science* **325**, 178–181 (2009).
4. Xia, Y. *et al.* Observation of a large-gap topological-insulator class with a single Dirac cone on the surface. *Nature Phys.* **5**, 398–402 (2009).
5. Qi, X. L. & Zhang, S. C. Topological insulators and superconductors. *Rev. Mod. Phys.* **83**, 1057 (2011).
6. Hsieh, D. *et al.* A tunable topological insulator in the spin helical Dirac transport regime. *Nature* **460**, 1101–1105 (2009).
7. Hsieh, D. *et al.* Observation of unconventional quantum spin textures in topological insulators. *Science* **323**, 919–922 (2009).
8. Roushan, P. *et al.* Topological surface states protected from backscattering by chiral spin texture. *Nature* **460**, 1106 (2009).
9. Xia, Y. *et al.* Observation of a large-gap topological-insulator class with a single Dirac cone on the surface. *Nature Phys.* **5**, 398–402 (2009).
10. Hsieh, D. *et al.* Observation of time-reversal-protected single-Dirac-cone topological insulator states in  $\text{Bi}_2\text{Te}_3$  and  $\text{Sb}_2\text{Te}_3$ . *Phys. Rev. Lett.* **5**, 146401 (2009).
11. Sato, T. *et al.* Direct evidence for the Dirac-cone topological surface states in the ternary chalcogenide  $\text{TlBiSe}_2$ . *Phys. Rev. Lett.* **105**, 136802 (2010).
12. Kuroda, K. *et al.* Experimental verification of  $\text{PbBi}_2\text{Te}_4$  as a 3D topological insulator. *Phys. Rev. Lett.* **108**, 206803 (2012).
13. Niesner, D. *et al.* Bulk and surface electron dynamics in a p-type topological insulator  $\text{SnSb}_2\text{Te}_4$ . *Phys. Rev. B* **89**, 081404 (2014).
14. Wolf, S. A. *et al.* Spintronics: a spin-based electronics vision for the future. *Science* **294**, 1488 (2001).
15. Kong, D. *et al.* Ambipolar field effect in the ternary topological insulator  $(\text{Bi}_x\text{Sb}_{1-x})_2\text{Te}_3$  by composition tuning. *Nature Nanotech.* **6**, 705 (2011).
16. Xiu, F. *et al.* Manipulating surface states in topological insulator nanoribbons. *Nature Nanotech.* **6**, 216 (2011).
17. McIver, J. W., Hsieh, D., Steinberg, H., Jarillo-Herrero, P. & Gedik, N. Control over topological insulator photocurrents with light polarization. *Nature Nanotech.* **7**, 96.
18. Johannsen, J. C. *et al.* Direct view of hot carrier dynamics in graphene. *Phys. Rev. Lett.* **111**, 027403 (2013).
19. Sobota, J. A. *et al.* Ultrafast electron dynamics in the topological insulator  $\text{Bi}_2\text{Se}_3$  studied by time-resolved photoemission spectroscopy. *J. Electron. Spectrosc. Relat. Phenom.* **195**, 249–257 (2014).
20. Sobota, J. A. *et al.* Ultrafast optical excitation of a persistent surface-state population in the topological insulator  $\text{Bi}_2\text{Se}_3$ . *Phys. Rev. Lett.* **108**, 117403 (2012).
21. Wang, Y. H. *et al.* Measurement of intrinsic Dirac fermion cooling on the surface of the topological insulator  $\text{Bi}_2\text{Se}_3$  using time-resolved and angle-resolved photoemission spectroscopy. *Phys. Rev. Lett.* **109**, 127401 (2012).
22. Crepaldi, A. *et al.* Ultrafast photodoping and effective Fermi-Dirac distribution of the Dirac particles in  $\text{Bi}_2\text{Se}_3$ . *Phys. Rev. B* **86**, 205133 (2012).
23. Wang, Y. H., Steinberg, H., Jarillo-Herrero, P. & Gedik, N. Observation of Floquet-Bloch States on the Surface of a Topological Insulator. *Science* **342**, 453 (2013).
24. Sobota, J. A. *et al.* Distinguishing bulk and surface electron-phonon coupling in the topological insulator  $\text{Bi}_2\text{Se}_3$  using time-resolved photoemission spectroscopy. *Phys. Rev. Lett.* **113**, 157401 (2014).
25. Hajlaoui, M. *et al.* Tuning a Schottky barrier in a photoexcited topological insulator with transient Dirac cone electron-hole asymmetry. *Nat. Commun.* **5**, 3003 (2014).
26. Kirilyuk, A., Kimel, A. V. & Rasing, T. Ultrafast optical manipulation of magnetic order. *Rev. Mod. Phys.* **82**, 2731 (2010).
27. Hsieh, D. *et al.* Selective probing of photoinduced charge and spin dynamics in the bulk and surface of a topological insulator. *Phys. Rev. Lett.* **107**, 077401 (2011).
28. Luo, C. W. *et al.* Snapshots of Dirac fermions near the Dirac point in topological insulators. *Nano Lett.* **13**, 5797 (2013).
29. Kim, S. *et al.* Robust protection from backscattering in the topological insulator  $\text{Bi}_{1.5}\text{Sb}_{0.5}\text{Te}_{1.7}\text{Se}_{1.3}$ . *Phys. Rev. Lett.* **112**, 136802 (2014).
30. Ishida, Y. *et al.* Time-resolved photoemission apparatus achieving sub-20-meV energy resolution and high stability. *Rev. Sci. Instrum.* **85**, 123904 (2014).
31. Sobota, J. A. *et al.* Direct optical coupling to an unoccupied Dirac surface state in the topological insulator  $\text{Bi}_2\text{Se}_3$ . *Phys. Rev. Lett.* **111**, 136802 (2013).
32. Cheng, P. *et al.* Landau quantization of topological surface states in  $\text{Bi}_2\text{Se}_3$ . *Phys. Rev. Lett.* **105**, 076801 (2010).

33. Hanaguri, T., Igarashi, K., Kawamura, M., Takagi, H. & Sasagawa, T. Momentum-resolved Landau-level spectroscopy of Dirac surface state in Bi<sub>2</sub>Se<sub>3</sub>. *Phys. Rev. B* **82**, 081305 (2010).
34. Jiang, Y. *et al.* Landau quantization and the thickness limit of topological insulator thin films of Sb<sub>2</sub>Te<sub>3</sub>. *Phys. Rev. Lett.* **108**, 016401 (2012).
35. Jiang, Y. *et al.* Fermi-Level tuning of epitaxial Sb<sub>2</sub>Te<sub>3</sub> thin films on graphene by regulating intrinsic defects and substrate transfer doping. *Phys. Rev. Lett.* **108**, 066809 (2012).
36. Reimann, J., Gdde, J., Kuroda, K., Chulkov, E. V. & Hfer, U. Spectroscopy and dynamics of unoccupied electronic states of the topological insulators Sb<sub>2</sub>Te<sub>3</sub> and Sb<sub>2</sub>Te<sub>3</sub>S. *Phys. Rev. B* **90**, 081106 (2014).
37. Sze, S. M. *Physics of Semiconductor Devices* (Wiley, New York, 1981).
38. Levinstein, M., Kostamovaara, J. & Vainshtein, S. *Breakdown Phenomena in Semiconductors and Semiconductor Devices* (World Scientific, London, 2005).
39. Nazarov, Y. V. & Danon, J. *Advanced Quantum Mechanics: A Practical Guide* (Cambridge University Press, Cambridge, 2013).
40. Fann, W. S., Storz, R., Tom, H. W. K. & Bokor, J. Electron thermalization in gold. *Phys. Rev. B* **46**, 13592–13595 (1992).
41. Li, T. *et al.* Femtosecond Population Inversion and Stimulated Emission of Dense Dirac Fermions in Graphene. *Phys. Rev. Lett.* **108**, 167401 (2012).

## Acknowledgements

The TrARPES measurements were jointly carried out by the Laser and Synchrotron Research Center of the Institute for Solid State Physics and the University of Tokyo (Proposal No. A181, A184). This work was partly supported by JSPS KAKENHI (Grant Numbers 23340105, 26800165).

## Author Contributions

S.Z., Y.I., K.K., K.S. and M.Y. performed the TrARPES experiment; S.Z. and Y.I. analysed the data and wrote the manuscript with A.K., J.W. and H.P. grew the samples; M.T., S.Q., S.S. and A.K. supervised the project.

## Additional Information

**Supplementary information** accompanies this paper at <http://www.nature.com/srep>

**Competing financial interests:** The authors declare no competing financial interests.

**How to cite this article:** Zhu, S. *et al.* Ultrafast electron dynamics at the Dirac node of the topological insulator Sb<sub>2</sub>Te<sub>3</sub>. *Sci. Rep.* **5**, 13213; doi: 10.1038/srep13213 (2015).



This work is licensed under a Creative Commons Attribution 4.0 International License. The images or other third party material in this article are included in the article's Creative Commons license, unless indicated otherwise in the credit line; if the material is not included under the Creative Commons license, users will need to obtain permission from the license holder to reproduce the material. To view a copy of this license, visit <http://creativecommons.org/licenses/by/4.0/>

# Supplementary Information for: Ultrafast electron dynamics at the Dirac node of the topological insulator $\text{Sb}_2\text{Te}_3$

Siyuan Zhu<sup>1,\*</sup>, Yukiaki Ishida<sup>2</sup>, Kenta Kuroda<sup>1</sup>, Kazuki Sumida<sup>1</sup>, Mao Ye<sup>3</sup>, Jiajia Wang<sup>4</sup>, Hong Pan<sup>4</sup>, Masaki Taniguchi<sup>1</sup>, Shan Qiao<sup>3,4</sup>, Shik Shin<sup>2</sup> & Akio Kimura<sup>1</sup>

<sup>1</sup>*Graduate School of Science, Hiroshima University, 1-3-1 Kagamiyama, Higashi-Hiroshima, Hiroshima 739-8526, Japan*

<sup>2</sup>*Institute for Solid State Physics, the University of Tokyo, 5-1-5, Kashiwa-no-ha, Chiba 277-8581, Japan*

<sup>3</sup>*State Key Laboratory of Functional Materials for Informatics, Shanghai, Institute of Microsystem and Information Technology, Chinese Academy of Sciences, 865 Chang Ning Road, Shanghai 200050, China*

<sup>4</sup>*Department of Physics, State Key Laboratory of Surface Physics, and Laboratory of Advanced Materials, Fudan University, Shanghai 200433, China*

## I Comparison of bulk and surface electron dynamics

To compare the electron dynamics of bulk and surface states, we altered the pump and probe delay and investigated the time dependent variations in the TrARPES images. Fig. S1(a) shows the difference image along the  $\bar{\Gamma}-\bar{K}$  line measured at  $t = 0.26$  ps. Here the bulk conduction band and two branches of UDC are represented as Bulk, Surface\_ A and Surface\_ B, respectively. We set energy and momentum frames and plotted the normalized intensity variation in each frame as a function of  $t$  [see Fig. S1(b)-(i)]. The intensities in the same energy range are normalized. The intensity variations of bulk and surface states do not show any significant differences. That tells us that the bulk and surface electron dynamics only depend on the energy.

## II Simulation of decay behavior from thermal distribution

Here we show how the excited electrons decay via electronic temperature cooling. First of all, we show the Fermi Dirac distribution function with a temperature  $T = T_0$  at the 'zero' delay time ( $t=0$ ), as shown in the inset panel of Fig. S2. Then we assume that  $T$  exponentially decays as described with  $T = T_1 + (T_0 - T_1) * \exp(-t/\tau)$ , where

$T_0$ ,  $T_1$  denote the initial and the equilibrium temperatures, and  $\tau$  expresses the decay rate. We plot the electron occupation probabilities at five binding energies  $E1$ ,  $E2$ ,  $E3$ ,  $E4$  and  $E5$  (marked in the inset panel) as shown in Fig. S2. We can find that the decay rate increases as the energy approaches the Fermi energy. The result of this simulation shows that the thermal decay cannot explain the observed population inversion.

### III Simulation of population inversion

To qualitatively demonstrate the population inversion, we draw the decay lines for the uniform DOS with the non-uniform one. Here we consider a simple model with 10 energy windows, marked as S0-S9. We assume that the electron transfer takes place only between the adjacent windows. The binding energy S9 is the highest and that of S0 is the lowest. The intensity of S0 is assumed to be caused only by a direct excitation. The intensity of S9 is considered to follow an exponential decay.

Considering a uniform DOS, as shown in the upper panel of Fig. S3 (c), we can simulate the decay lines of different windows. As shown in Fig. S3 (a), the high binding energy window shows the earlier rising edge. Therefore the uniform DOS cannot be the origin of the population inversion.

The non-uniform DOS, where the DOS in the region S7 is reduced down to 10% of the others is assumed for the simulation as shown in the lower panel of Fig. S3 (c). Here, all the other parameters are set to the same values as those used for the uniform DOS. As shown in Fig. S3 (b), a big change occurs for the regions S6-S8, while the higher energy regions do not change significantly. The intensity of S8 shifts to earlier delay time than that of S6, just like what we experimentally observed for UDC and LDC. This result can reasonably explain that the observed population inversion takes place due to the bottleneck effect near Dirac node.

**Figure S1: Decay behaviors of bulk and surface electrons** (a) The difference image at  $t = 0.26$  ps. The bulk conduction band and two branches of UDC are marked as Bulk, Surface\_ A and Surface\_ B, respectively. (b)-(i) The decay behaviour of Bulk, Surface\_ A and Surface\_ B at different energy ranges (340-360 meV, 360-380 meV, 380-400 meV, 400-420 meV, 420-440 meV, 440-460 meV, 460-480 meV and 480-500 meV).

**Figure S2: Simulation of decay behavior from thermal distribution** The intensity variation lines at different binding energy E1, E2, E3, E4 and E5, as marked in the inset panel, which shows the thermal distribution at a delay time of 0ps.

**Figure S3: Simulation of a simple model for hourglass effect** (a) Simulated decay lines assuming a uniform DOS distribution. (b) Simulated decay lines assuming 10% DOS at energy region S7. (c) Schematic figures for the assumed DOS distributions in the simulation.

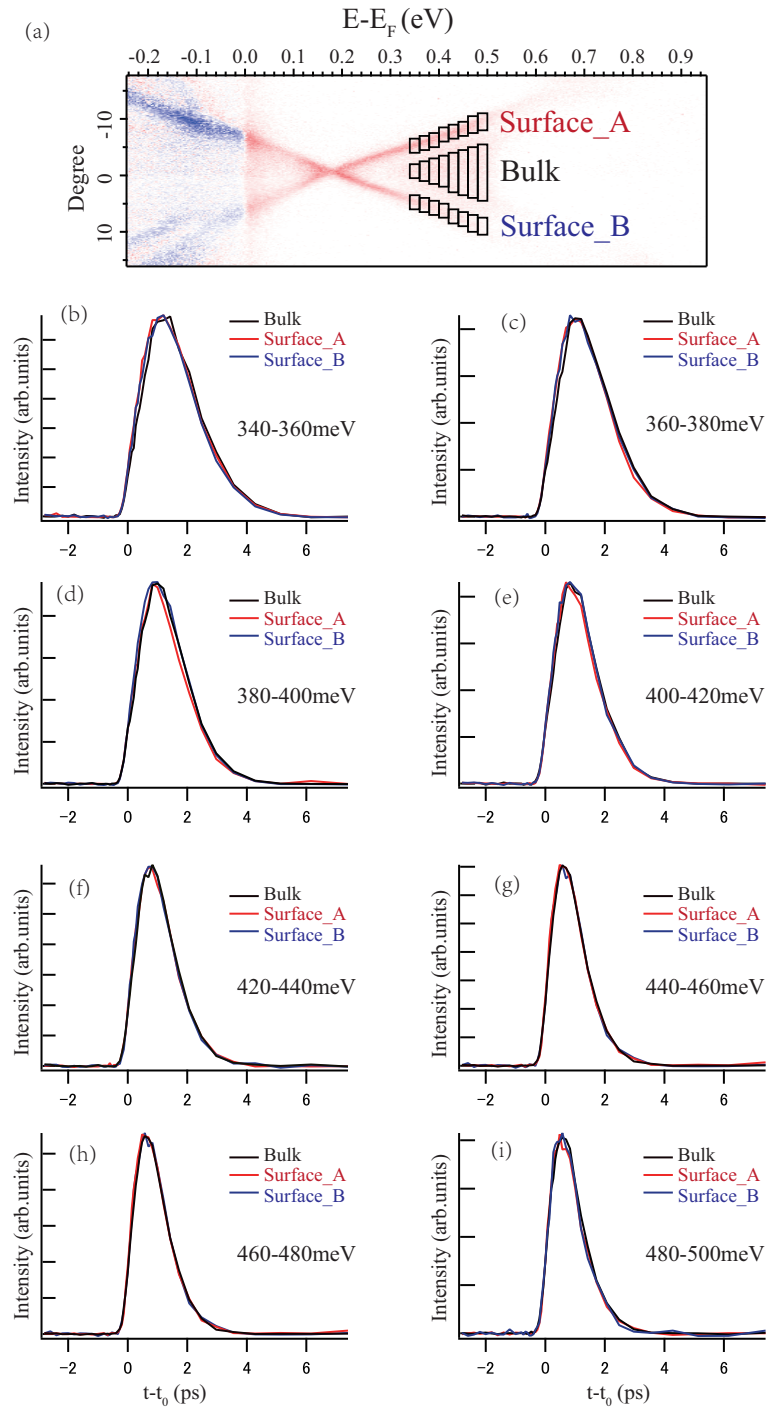


Figure 1:



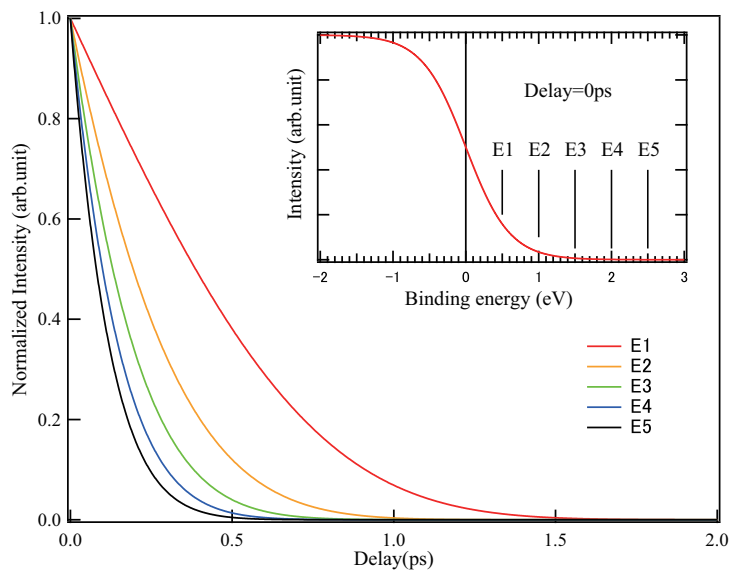


Figure 2:

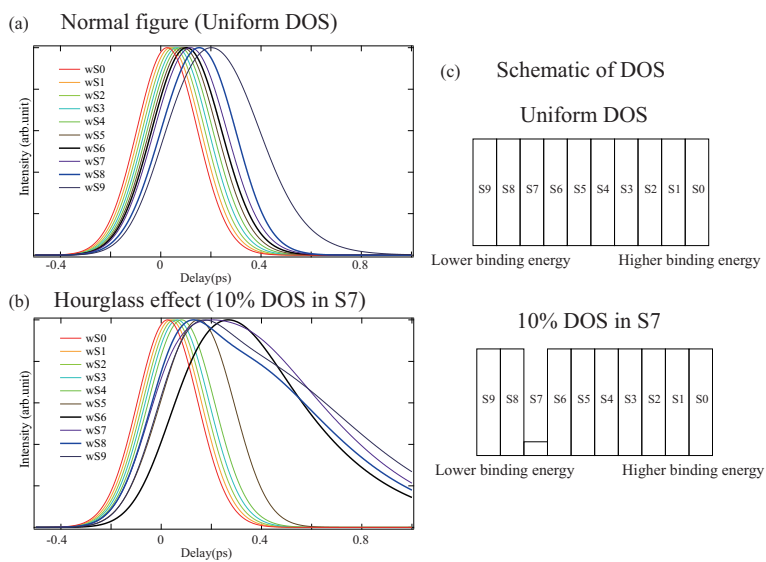


Figure 3: